An Accurate and Transferable Machine Learning Potential for Carbon

Patrick Rowe[1], Volker L. Deringer[2], Piero Gasparotto[1], Gábor Csányi[3], and Angelos Michaelides[1,a]

[1]Thomas Young Centre, London Centre for Nanotechnology, and Department of Physics and Astronomy, University College London, Gower Street, London, WC1E 6BT, U.K.
[2]Department of Chemistry, Inorganic Chemistry Laboratory, University of Oxford, Oxford OX1 3QR, U.K.
[3]Engineering Laboratory, University of Cambridge, Trumpington Street, Cambridge CB2 1PZ, U.K.
[a]Author to whom correspondence should be addressed: angelos.michaelides@ucl.ac.uk

June 25, 2020

Abstract

We present an accurate machine learning (ML) model for atomistic simulations of carbon, constructed using the Gaussian approximation potential (GAP) methodology. The potential, named GAP-20, describes the properties of the bulk crystalline and amorphous phases, crystal surfaces and defect structures with an accuracy approaching that of direct *ab initio* simulation, but at a significantly reduced cost. We combine structural databases for amorphous carbon and graphene, which we extend substantially by adding suitable configurations, for example, for defects in graphene and other nanostructures. The final potential is fitted to reference data computed using the optB88-vdW density functional theory (DFT) functional. Dispersion interactions, which are crucial to describe multilayer carbonaceous materials, are therefore implicitly included. We additionally account for long-range dispersion interactions using a semianalytical two-body term and show that an improved model can be obtained through an optimisation of the many-body smooth overlap of atomic positions (SOAP) descriptor. We rigorously test the potential on lattice parameters, bond lengths, formation energies and phonon dispersions of numerous carbon allotropes. We compare the formation energies of an extensive set of defect structures, surfaces and surface reconstructions to DFT reference calculations. The present work demonstrates the ability to combine, in the same ML model, the previously attained flexibility required for amorphous carbon [*Phys. Rev. B*, **95**, 094203, (2017)] with the high numerical accuracy necessary for crystalline graphene [*Phys. Rev. B*, **97**, 054303, (2018)], thereby providing an interatomic potential that will be applicable to a wide range of applications concerning diverse forms of bulk and nanostructured carbon.

1 Introduction

The same characteristics which make carbon a fascinating element for study also make it challenging to model computationally. It exhibits some of the greatest structural diversity - and associated diversity of properties - of any of the elements [1–7]. Its allotropes range from zero to three-dimensional, have metallic, semiconducting and insulating phases and boast mechanical properties including some of the highest tensile strengths, hardnesses and bulk moduli measured [8, 9]. It is unsurprising, therefore, that carbon is considered to be not just an element of prime technological importance, but also remains the subject of continued fundamental scientific study [10–16].

Current applications of elemental carbon are numerous, they include lightweight and strong structural materials, anodes of batteries and components in advanced optical technologies [9, 13, 16–19]. The usefulness of elemental carbon has also clearly not yet been exhausted; future applications propose to make use of graphene's unique electronic properties for advanced electronics [11, 20], carbon nanotubes' structural and optical characteristics for performance materials [18, 21] and the thermal and optical properties of diamonds for laser optics [9, 22, 23], amongst innumerable other examples.

Atomistic simulations have played a major role in developing our understanding of carbon materials. Among the many scientific problems that have been addressed with carbon potentials, we may mention the wear process of diamond [24] or the compression behaviour of glassy carbon [25]. The first many-body interatomic potential for modelling carbon was published in 1988 by Tersoff. This potential was used to investigate the properties of carbon's crystalline and amorphous allotropes [26]. The reactive empirical bond order (REBO, REBO-II) potentials built on the original Tersoff formulation to include a wider range of parameters and data in the fit, as well as adding additional conjugation and torsional terms, and modifying the bond order expression for small angles [27, 28]. However, the Tersoff and REBO-II potentials only considered nearest neighbour interactions and did not account for the effects of dispersion. The adaptive intermolecular REBO (AIREBO) potential [29] sought to correct this by adding an additional long-range Lennard-Jones term between atoms with larger separations, while making no modifications to the short-range part of the potential. The long-range carbon bond order potential (LCBOP) not only increased the range of the potential to account for longer-range interactions but also constituted a complete reparameterisation of the bond order potential to improve the accuracy and transferability of the model, though long-range dispersion interactions are still omitted [30].

Further developments, beyond the scope of detailed discussion here, include the LCBOP-II potential which expanded the application range of the model to include the liquid phase [31, 32], the environment dependant interatomic potential (EDIP) for carbon [33] which employed properties calculated from *ab initio* simulation in its parameterisation, the introduction of a dynamic cutoff to bond-order potentials [34] and a recent reparameterisation of a carbon ReaxFF potential [35]. Notwithstanding the long-standing success of these potential models, there are inherent limitations to even the most advanced of them. Such issues are particularly relevant when one departs from the idealised structures (diamond, graphite, *etc.*), as shown in two detailed benchmark studies by de Tomas et al. [36, 37].

Machine learning (ML) has recently arisen as a way of addressing some of these limitations. A number of practical approaches for modelling the potential energy surface (PES) using ML have been developed in recent years, employing algorithms including artificial neural networks, Gaussian process regression, and compressed sensing [38–45]. The demonstrated ability of ML algorithms to fit arbitrary functions with an extremely high accuracy [46], combined with recent developments in high-dimensional descriptors for atomic systems makes ML approaches for the development of interatomic potentials an increasingly popular approach [42, 47–50]. Indeed, the use of machine learning methodologies to model carbon has a significant precedent. Some of the first examples of ML potentials, using both Gaussian process regression and artificial neural networks, were fitted for graphite and diamond, these were tested with regards to properties off the crystalline phases and the graphite-diamond phase coexistence line [38, 39, 51]. One of the first neural-network potentials was used for large-scale simulations of the diamond nucleation mechanism [52]. We recently introduced a machine learning potential for pristine graphene constructed using the Gaussian approximation potential (GAP) framework, which achieved excellent accuracy when benchmarked against DFT and experiment for a wide range of lattice and dynamical properties, including the phonon dispersion relations, thermal expansion and Raman spectra at different temperatures [53].

While achieving good accuracy in a specific region of configuration space is not trivial, the problem of the transferability of a potential is much more challenging to solve from a ML perspective. In 2017, some of us reported a highly transferable GAP model trained primarily on the amorphous and liquid phases of carbon (henceforth termed GAP-17), based on DFT-LDA reference data. The focus, there, was somewhat complementary—to be able to describe very diverse structural environments, albeit accepting a degree of numerical error. As an example, the in-plane force errors for a pristine graphene sheet are 0.03 eV Å^{-1} with the graphene-only GAP mentioned above, as compared to 0.27 eV Å^{-1} with GAP-17. For comparison, these errors for a range of commonly used empirically fitted potentials range from 0.6 to 3.1 eV Å^{-1} (more details are in Ref. [53]). In return, owing to the flexibility and transferability ensuing from its choice of reference database, GAP-17 enabled the study of a num-

ber of scientific problems which involve diverse structural environments, including understanding the mechanism of growth of sp^3 hybridised amorphous carbon by ion deposition [54], extensive studies of the surface properties (and chemical reactivity) of tetrahedral amorphous carbon [54–56], the structure of "porous" carbonaceous materials which are relevant to applications in batteries and supercapacitors [57, 58], and crystal-structure prediction [5].

The model we present here, GAP-20, builds on all of the previous work applying the GAP machine learning methodology to the development of carbon potentials, to achieve the accuracy required for capturing subtle differences in formation energies of nanostructures or in defect formation energies, and for describing phonon dispersions to within meV accuracy - while maintaining the flexibility and transferability of GAP-17. Importantly, all data are generated using a dispersion-corrected DFT method which properly accounts for longer-range interactions in low-dimensional carbon structures, and the fitting architecture is adapted to account for those. Our tests suggest GAP-20 to be suitable as a "general-purpose" carbon ML potential for diverse areas of study.

While detailed discussions of the construction and testing of the potential will be given in subsequent sections, we take a moment to highlight the main points here. The composition of the training data set and performance of this potential is summarised in figure 1. GAP-20 correctly predicts the formation energies of diamond, graphite, fullerenes and nanotubes, to an accuracy of a few meV, and achieves comparable accuracy for a number of crystalline and amorphous surfaces. The computed formation energies of defects are also accurate, with overall errors significantly lower than those obtained from comparable empirical models. At the same time, GAP-20 can accurately predict the behaviour of high temperature liquid carbon over a wide range of temperatures and densities, which will be shown below. We believe that these features make GAP-20 a useful tool for the accurate modelling of nanostructured carbons; nanotubes, graphitised carbon and materials with varying degrees of defects and disorder.

The rest of the paper will be organised as follows. We first describe our process for the construction of a training set suitable for developing such a potential. We then give details on the construction and training of the model itself, with discussion of particular aspects which required special attention or optimisation. Subsequently, we present an extensive and rigorous testing of our model, for a wide range of properties. We also compare the results of our model to a selection of commonly used empirical potentials which model the interatomic interactions in carbon with differing degrees of simplification. Specifically we choose the Tersoff, REBO-II, AIREBO and LCBOP models. The selection of potentials considered here is by no means exhaustive and is only intended to give some basis for comparison between previous work

and the model we introduce, as well as illustrating how the inclusion or exclusion of different interactions (e.g. dispersion interactions) may affect the performance of a model. A more detailed benchmarking across a wider range of potentials, complementing the existing detailed tests for amorphous and "graphitised" carbons [36], may be the subject of future work.

2 Generation and Selection of Training Data

One of the challenges inherent in constructing a generalised potential for carbon is the enormous variety of structures which must be considered. In addition to its more commonly encountered crystalline phases; diamond and graphite, carbon may be found in forms of differing dimensionality, from zero dimensional fullerenes, to one dimensional nanotubes, two dimensional graphene and three dimensional amorphous forms [6].

Specifically in the case of ML, one is drawn to the problem of the composition of the large database of example configurations, known as the training data set. For a potential to be both accurate and transferable, its training data set ought to include representative configurations from all of the thermally accessible chemical space. One might initially suggest that the problem is therefore intractable, if in order to produce a potential which is capable of accurately modelling all of the relevant phases of carbon, we must explore the entirety of the vast 3N-dimensional chemical space. It is an empirical observation, however, that the thermally accessible and physically relevant regions of this chemical space constitute a vastly reduced subset of all of the available configurations [59–61]. Further, rather than an exploration of the 3N dimensional space, in fitting the parameters of a ML algorithm we are primarily concerned with an exploration of the reduced dimensionality descriptor space [59, 62–64]. In the case of atom centred descriptors such as the smooth overlap of atomic positions (SOAP), this represents the local environment around a particular atom rather than the global structure [63]. While the structural variability of carbon is globally almost infinite, many of these structures are constructed from similar local motifs, for example the tetrahedral building blocks of diamond [65, 66]. Similar logic may be applied to more complex structures.

The reference configurations which comprise our structural database are drawn from a wide variety of sources. Regardless of the origin of the configuration itself (e.g., from the GAP-17 database), its properties, those being the total energy, atomic forces and virial stresses, which comprise the actual training data, are always computed using the same level of tightly converged plane-wave DFT including dispersion corrections. We use the VASP plane-wave DFT code, we perform spin-polarised calculations with the optB88-vdW dispersion inclusive exchange-correlation functional [67–70], a
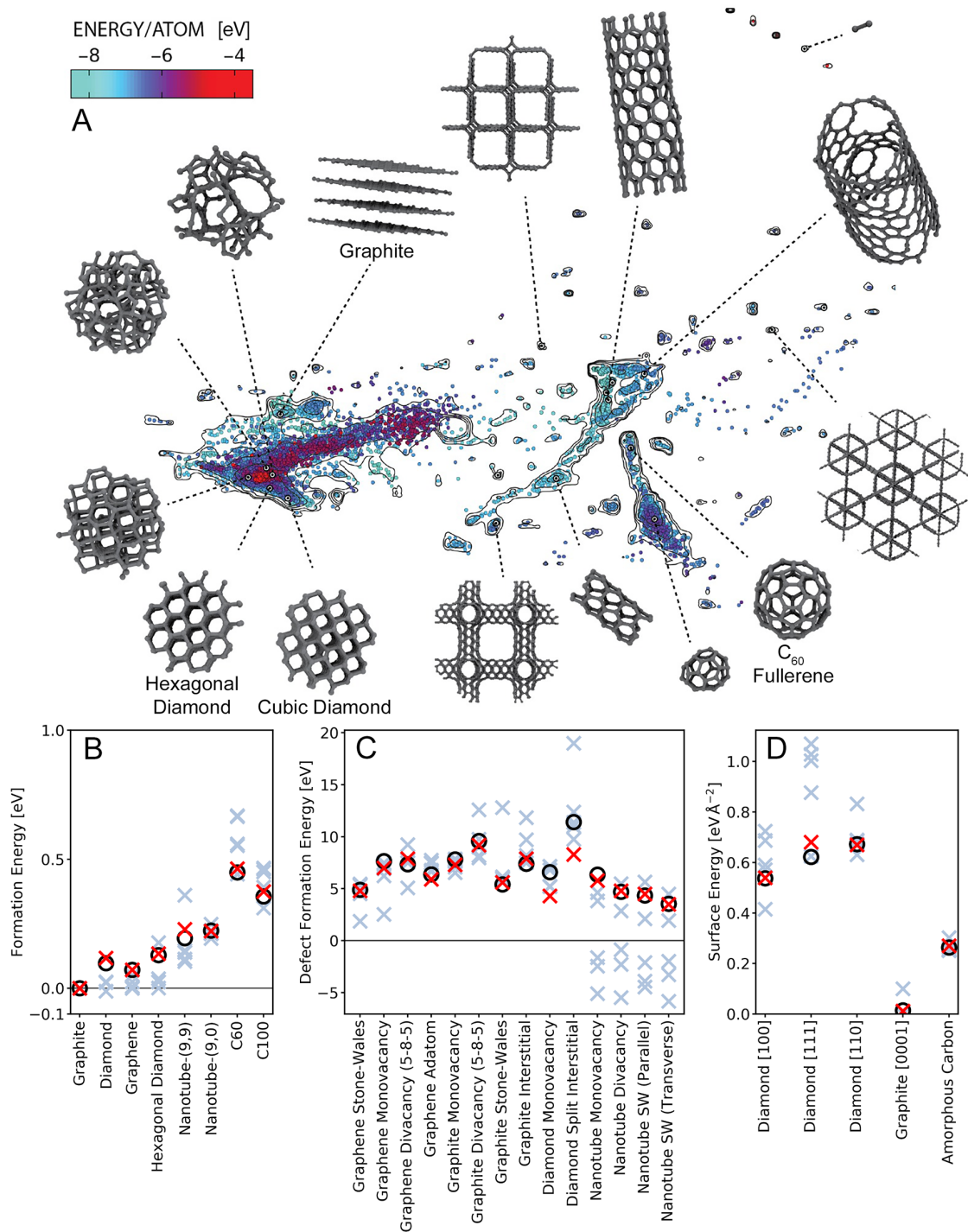
Figure 1: Overview of some of the key structures included in the training shown through a sketch-map representation (top) as well as selected information on the performance of the potential for a variety of properties. (a) Sketch-map representation of the total data set for carbon generated as part of this work. Select structures are identified for graphite, diamond, hexagonal diamond (Lonsdaleite), amorphous carbon and fullerenes. Points are coloured according to their energy, while contours indicate the density of the database population in a particular region. Bottom, is a summary of (b) the predicted crystalline formation energies, (c) defect formation energies and (d) surface energies, comparing the DFT (optB88-vdW) reference (black circles) GAP-20 (red crosses) and all other models (blue crosses).

plane-wave cut-off of 600 eV and a projector augmented wave pseudopotential [71–73]. A Gaussian smearing of 0.1 eV is applied to the energy levels and dense reciprocal space Monkhorst-Pack grids are used [74]. In the case of the reduced dimensionality allotropes; graphene and nanotube structures, the reciprocal space sampling is only performed in the directions in which the allotrope is periodic. The properties of fullerene structures are calculated at the gamma point. For this potential, we choose the optB88-vdW functional as it has already been demonstrated to provide an excellent description of carbonaceous materials, in particular graphitic carbon – for which its prediction of the binding energy and interlayer spacing is in good agreement with experimental values [75].

The database of configurations presented here uses as its foundation a combination of the training data sets for the two carbon potentials previously published primarily for liquid and amorphous carbon (GAP-17), and for pristine graphene, respectively [53, 62]. A large number of new configurations are considered in addition to these existing ML data sets [5, 6, 76]. We endeavour to comprehensively cover all the possible crystalline phases of carbon found at moderate temperatures and pressures, including more exotic allotropes. To that end, DFT optimised structures for graphite, graphene, cubic and hexagonal diamond are included, as well as the structures of a library of fullerenes comprised of fewer than 240 atoms and all nanotube structures with chiral indices, $3 \leq n, m \leq 10$ with fewer than 240 atoms in their unit cell. Optimised structures are also included for the SACADA database of exotic carbon allotropes [76] and the results of a GAP-17 driven random structure search [5]. In addition to bulk or pristine phases, the structures of relevant low Miller-index faces of the crystalline phases are included, along with a large number of important defect structures [77–84].

For all of these structures, we have performed some *ab initio* and some iteratively improved GAP driven molecular dynamics simulations at a number of temperatures so as to also sample the region of phase space close to these local minima [53, 62]. The resulting database is comprised of ca. 17000 configurations each containing from 1 to 240 atoms per cell.

The choice of which structures might be important for training a potential requires for the most part chemical or physical intuition on the part of the researcher [42, 59, 85]. Some of these choices may be clear, for example the need to include configurations representing the bulk structures of diamond and graphite. Others, however, such as the inclusion or exclusion of particular defect or surface structures, will depend on the desired application of the potential (and, to some extent, on personal choice). To maximise the transferability of our model, we have produced as comprehensive a database as possible – too large to train on with current computational facilities. Rather than using the full database for sparsification, as commonly done in GAP fitting (including in

the development of GAP-17), we instead allow the bulk of our training configurations to be chosen from the total dataset using a sampling method known as farthest point sampling (FPS) [42, 86]. Within this set, we then carefully check the data saturation of our training with respect to the number of sparse points, which is discussed in section 3.

This method allows us to start with a much more comprehensive database than previously, while still keeping the computational effort at the fitting stage tractable. We wish for our training dataset to have the widest possible sampling of descriptors and forces – leaving no physically relevant configurations unsampled, while avoiding overrepresentation of particular regions of phase space. FPS facilitates this, by allowing a selection of frames to be made based on a measure of the global similarity (in descriptor space) between possible configurations [42, 86]. Given a set of n descriptors of type d for a number of frames, $\mathbb{Q} = \{\mathbf{q}_{i=1...n}^{d,avg}\}$, which are themselves the average of the individual descriptors of the atoms in a particular frame $\mathbf{q}_i^d$, the FPS algorithm selects configurations so that at each step, the kernel distance between previously selected configurations $\mathbb{Q}_{selected} = \{\mathbf{q}_1^{d,avg} \dots \mathbf{q}_m^{d,avg}\}$ and the new configuration $\mathbf{q}_{m+1}^{d,avg}$ is maximised. That is,

$$\mathbf{q}_{m+1}^{d,avg} = \mathrm{argmax}_{\mathbf{q}^{d,avg}}[\mathrm{D}(\mathbb{Q}_{selected}, \mathbf{q}^{d,avg})], \qquad (1)$$

where D is the kernel distance between the selected descriptors (and associated frames) $\mathbb{Q}_{selected}$ and the candidate descriptor $\mathbf{q}^{d,avg}$. In our case, we use the SOAP descriptor as a structural fingerprint of a configuration and the dot product between two SOAP descriptors as our kernel similarity measure [63]. As has previously been shown for molecular systems, we find that this method of selection enables the training of a potential which demonstrates good transferability [59]. However, due to the nature of the sampling, it lacks the dense population of configurations around particular local minima which we find are important for achieving very high accuracy on particular crystalline properties. We therefore choose to augment the training dataset selected through FPS with a number of mandatory configurations chosen using chemical intuition, focused on the bulk crystalline phases and certain defect and surface structures. Specifically, we note that optimised geometries for structures used in the validation sections of this paper are included in the training. The final database is comprised of the union of the 4000 FPS-selected points and the existing GAP-17 dataset, while a further ca. 1000 configurations are manually added to target specific properties.

The selected configurations, as well as a representation of their position in phase space, can be seen illustrated in figure (Fig. 1). This sketch-map [86, 87] representation of the total training dataset uses the same measure of kernel similarity as discussed above to position points in a reduced dimensionality such that points which are similar

in the full high-dimensional descriptor space are closer together, and those which are dissimilar are further apart.

This sketch-map representation also serves as a qualitative overview of the type of structures to which we fit our model. Structures with carbon atoms of highly varied coordination environments, from sp^1 to sp^2 and sp^3 can be seen. Those allotropes which are sp^2 hybridised, such as graphene, graphite and carbon nanotubes are clustered together towards the right of the map. Amorphous structures can be seen as a large region in the centre, with low density (sp^1 and sp^2 rich) amorphous carbon at the far right, high density sp^3 rich amorphous carbon towards the left, eventually approaching crystalline diamond at the very far left of the map. The more exotic, sometimes hypothetical structures collected from the SACADA database are often found separated from bulk crystalline or amorphous configurations. In the far top right of the map, isolated gas phase dimer configurations are found.

3   Training of the Potential

We choose to construct GAP-20 to represent the PES as the combination of contributions from a two body (2b), a three body (3b) and a high dimensional many-body (MB) component. It is an empirical observation that a large proportion of the interaction in an atomistic system may be satisfactorily captured by considering 2b interactions. In particular this is the case for the exchange repulsion experienced as interatomic distances become very small. Representing this exchange repulsion in its full high-dimensional form would be costly from the perspective of both training data generation, potential generation and the ultimate evaluation of the potential. The nature of bonding interactions for carbon may also be captured in an approximate way, being generally attractive between 1.2 - 1.6 Å, with an attractive tail at long distances. We design the 2b part of our model as a GAP fitted 2b component (V_{short}) r < 4.0 Å. For larger separations ($10 \geq r > 4.0$ Å), this smoothly transitions to an analytical spline potential (V_{long}) which decays as r^{-6}. This long range component is fitted to correctly reproduce (albeit without many-body contributions) the long-range attraction due to van der Waals interactions of graphitic layers. A smooth transition is achieved by first fitting the analytical form of V_{long} to the graphene bilayer interaction curve from 3.0 to 10.0 Å. V_{short} is then trained by first subtracting V_{long} from the total energy and fitting to the difference. The resultant 2b potential (Fig. 2) simply has the final form $V_{short} + V_{long}$

The true subtleties of interatomic bonding are inherently many-body in character, however. We represent these higher-order contributions to the potential energy using a combination of a 3b descriptor and the aforementioned SOAP descriptor. The full details of the construction of the 3b and SOAP descriptors is given in detail
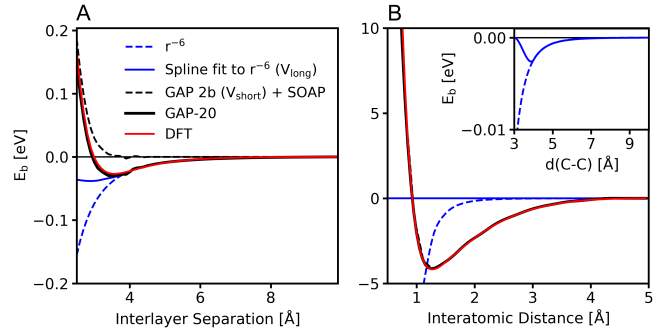
elsewhere [53, 62, 63, 88–91].

Figure 2: Construction of the long-range 2b component of the GAP model. An analytical spline is fitted to a function which decays as r^{-6}, designed to recover the long-range attraction between graphene layers. (a) Shows the predicted energies for each component for the interaction of two graphene layers at different distances. The long range attraction is well characterised by the r^{-6} component of the r^{-6} potential, which is in turn well recovered by the analytical spline. The GAP fit using a 2b, (V_{short}), 3b and SOAP descriptor provides the appropriate repulsive potential at short distances but is too short ranged to describe the attractive tail. GAP-20 reproduces the whole curve with good accuracy across a range of distances. (b) Shows the same decomposition for the gas phase dimer. In this case, the strong bonding interactions are dominated by the GAP 2b (V_{short}), 3b and SOAP descriptor components. The energy of the r^{-6} component becomes large and negative for short distances. (b, inset) Provides a closer view of panel B, and shows how the 2b spline fit to the r^{-6} component is brought smoothly to 0 at a distance of 3 Å.

In short, the 3b term is a symmetrized transformation of the Cartesian coordinates of triplets of atoms, which is designed to be permutationally invariant to the swapping the atomic indices [53, 62]. In the construction of the SOAP descriptor, the local environment around a target atom is represented by a 'local neighbour density', constructed by placing a Gaussian basis function on each neighbouring atom within a certain cutoff, which we choose to be 4.5 Å. The Gaussian basis functions are scaled by a factor of $1/r^{0.5}$ to reflect the greater contribution to material properties of atoms which are closer together [92–94]. Other functional forms for the radial scaling exist and the introduction of this scaling was performed independently of the optimisation of the SOAP descriptor cutoff, the choice of which is motivated below. As a result, there may still be scope for further optimisation of these parameter sets beyond what is performed here. The local neighbour density is expanded in a basis set of spherical harmonics, the coefficients of which form a 'SOAP vector'. In our case we use a basis set up to order l = 4 and n = 12, our motivation for which is

discussed in the following paragraph. This SOAP vector constitutes a unique representation of the local environment, which satisfies the requirements of being translationally, rotationally and permutationally invariant. The SOAP kernel, used for regression, is constructed as the scalar product of individual SOAP vectors. Such a kernel is physically interpretable, as it corresponds directly to the integral of two neighbour densities for all possible 3D rotations. Details for the specific choices for a number of associated hyper-parameters are given in the supplementary material, while further details on their significance is given elsewhere [39, 53, 62, 63, 88–91].
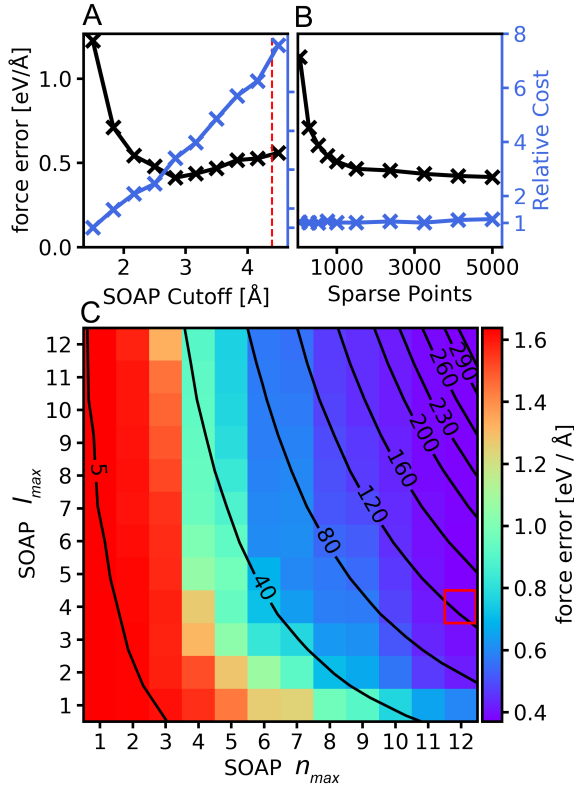

Figure 3: Mean absolute force errors calculated for an independent test set of configurations for different SOAP descriptors. (a) Force error behaviour and cost of evaluation (relative to the fastest GAP) of the resultant model as a function of the SOAP descriptor cutoff, the selected value of 4.5 Å is indicated by the dashed red line. (b) Force error convergence and relative cost as a function of the number of sparse points included in the training. (c) Dependence of the force error and model evaluation cost on the order of the SOAP neighbour density basis set expansion. Force errors are indicated by the colour bar, while relative costs are shown by contour lines, our choice $l_{max} = 4$, $n_{max} = 12$ is highlighted by the red square.

We now provide the details of select convergence tests for the optimisation of our GAP model. These tests consider the independent optimisation of the SOAP descriptor cutoff, number of sparse points and the order of the radial basis set expansion. In general we begin with a SOAP descriptor with an expansion of the neighbour density up to $l_{max} = 8$, $n_{max} = 8$, a cutoff of 4.2 Å, $\sigma_{force} = 0.01$ eV Å^{-1} and $\sigma_{energy} = 0.001$ eV and $\zeta = 4$. We modify one parameter at a time in isolation, while keeping the remainder fixed. We calculate the force error for the resulting models on a randomly selected independent set of test configurations which is not included in the training.

Figure 3(a) shows the behaviour of the force errors as a function of the SOAP descriptor cutoff. The force error has a minimum for a cutoff of 2.9 Å, after which it begins to rise again as the increased size of the descriptor space expands beyond what can be populated with the number of available training configurations. A naïve optimisation of these parameters based purely on the force errors would therefore select a cutoff radius of 2.9 Å. However, selection of these parameters cannot be performed in isolation from the intended application of the potential, but must also be motivated by knowledge of the behaviour of the material of interest. In this regard, the force (or energy) error alone may be regarded as an imperfect or incomplete target property for optimisation. Specifically, we find that although the minimum in the force error is found at much shorter distances, a longer cutoff of 4.5 Å must be used in order to correctly describe graphitic structures, a feature which we consider to be mandatory for this potential. The inter-layer spacing of graphitic structures is typically large (approx. 3.3 Å) and a potential must incorporate enough of the structure of both layers to correctly model properties such as the binding curve of graphene layers or the energy difference between AA and AB stacked graphite. The effect of these short cutoffs can be seen in the unsatisfactory behaviour of the Tersoff and REBO-II models when modelling the inter-layer spacing of graphite (Table 1), or graphene bilayers (Supplementary fig. 6). However, the problem of producing a single analytical metric for optimisation, which satisfactorily includes properties such as the lattice parameters, defect formation energies or phonon errors as well as the force errors themselves is a challenging one. In this instance, the design choice of selecting an appropriate descriptor cutoff remains partly qualitative in nature.

Figure 3(b) shows the convergence of the mean absolute force errors as a function of the number of sparse points used in the training, this may be considered as a measure of the data saturation of GAP-20. The force errors decrease rapidly up to approx. 1500 sparse points, at which point they begin to level off, although we note that a further increase in the number of sparse points has a negligible impact on the cost of evaluating the model. Our choice of 9000 sparse points is therefore very tightly converged.

In figure 3(c) we show how the force error for our model converges as a function of the order of the basis set of radial functions used to expand the SOAP neighbour density. The relative computational cost of each basis set is indicated on the same plot by labelled contour lines.

We find that the radial (n) component of the expansion, typically has a greater impact on the rate of convergence than the angular (l) component. While previously in the construction of GAP models, band limits $n_{\max} = l_{\max}$, were used for the SOAP descriptor, we find that surprisingly, an improvement in accuracy can be achieved with essentially no additional cost by making a selection for the basis set expansion which is strongly biased to the radial ($n_{\max}$) component. Of course the cost must also be taken into account, the use of a larger radial component is more expensive than an identical increase in the angular component, due to the greater number of basis functions introduced. Our selection of $l_{\max} = 4$, $n_{\max} = 12$ is chosen as a compromise between accuracy and efficiency. Although a small improvement in the force errors can be achieved by selecting $n_{\max} = 12$, $l_{\max} > 4$, the resultant increase in the cost of training restricts both the size of the training data set which can be used and the size and length scales to which the resultant potential can be applied.

4   Crystalline Carbon

Among the most important material properties for any potential to predict accurately are those of the bulk crystalline phases. Table 1 compares the lattice parameters and bond lengths as predicted by GAP-20 to those from the reference DFT method, in addition to a number of empirical models. In figure 4, we also provide both the atomisation energies, and the formation energies of the crystalline phases relative to the thermodynamically stable state of carbon (at standard temperature and pressure), i.e. graphite. We define the atomisation energy of a phase relative to the isolated gas phase carbon atom E_{at} as,

$$E_f = E_{\mathrm{bulk}} - nE_{\mathrm{at}}, \qquad (2)$$

where E_{bulk} is the energy of the bulk phase and n is the number of atoms in the bulk. Lattice parameters are calculated by independently optimising the cell vectors for each allotrope, until the total energy is converged to less than 10^{-4} eV. GAP-20 accurately predicts the lattice parameters and bond lengths of all of the tested crystalline allotropes with an average error of 0.2%, and their formation energy to within 0.5%.

Accurately modelling the graphite c lattice parameter, corresponding to the spacing between graphitic layers proved particularly challenging for candidate GAP models, as did the formation energy. This is in large part due to the shallow nature of the energetic minimum characterising the graphite inter-layer interactions and the long range of the atomic descriptor required to capture it. As discussed above, the choice of SOAP cut-off was specifically informed by a desire to capture this property correctly. We consider this in particular to be a mandatory

characteristic of a general carbon potential which would be absent for any model with a shorter cut-off.

It is useful here to make a brief comparison to selected empirical potentials. While we do include DFT reference data for all properties, in subsequent sections these reference values are only computed using the same level of DFT used to train GAP-20. For benchmarking GAP-20, which is our primary purpose, this is not problematic, however we do not fully account for the potential impact of functional dependence, or the errors of DFT with respect to experiment, when making comparisons to empirical models. Many of the empirical models considered are fitted to experimental data, or contain values from other DFT functionals, typically LDA, which should be taken into account when comparing different model predictions to our optB88-vdW reference values. To give some indication of the functional dependence, reference values for the formation energies in figure 4 are given using both the optB88-vdW and LDA functionals. We also re-iterate that the GAP-17 model was fitted to LDA data, so it would be expected to accurately reproduce DFT values at this level only.

On average, GAP-20 predicts the lattice parameters of the tested crystalline phases with an error of 0.2%, while the Tersoff, LCBOP, REBO-II, AIREBO potentials have errors averaging 5%, 0.3%, 4% and 1% respectively (Table 1. What the Tersoff and REBO-II potentials gain in efficiency by using short cutoffs, they lose in accuracy, notably by predicting dramatically incorrect inter-layer spacings (c lattice parameters) for graphite. This error is fixed by the inclusion of medium and long-range terms to account for van der Waals interactions in the LCBOP and AIREBO models, however. Despite its inaccuracy for graphene, the REBO-II potential does achieve good accuracy on the remaining lattice parameters; the additional terms included in the bond-order potential constitute a dramatic improvement over the Tersoff potential. Due in part to its complete reparameterisation to account for the effects of long-range interactions in the bond-order part of the potential, LCBOP does outperform the other empirical potentials tested here in most cases.
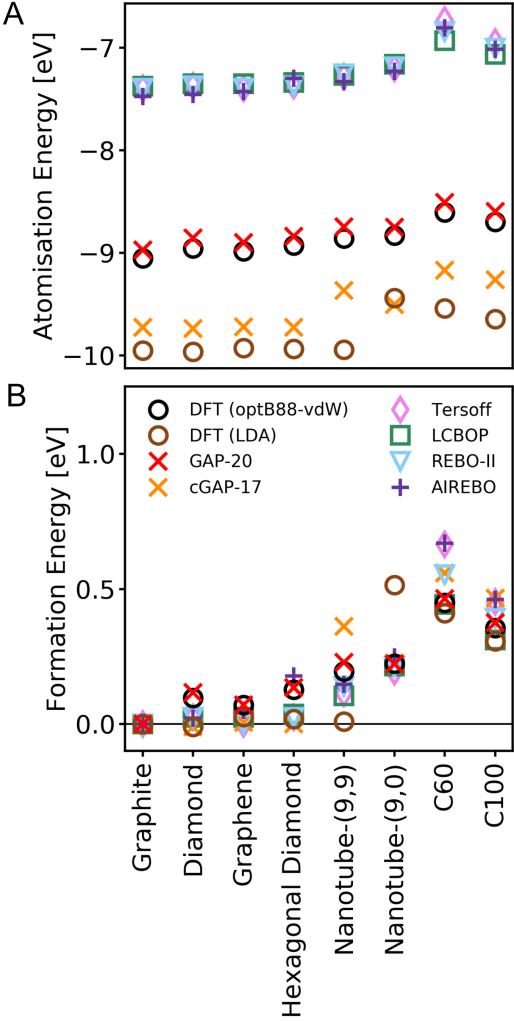
Figure 4: Formation energies of the crystalline phases of carbon, comparing results from DFT (optB88-vdW and LDA) to those from GAP-20 and the other models tested. (a) Atomisation energies using the isolated gas phase carbon atom as a reference, differences are dominated by overstabilisation of the gas phase atom by empirical models. (b) Formation energies given relative to the graphite formation energy of each particular model.

In absolute terms, the atomisation energies (fig. 4(a)) from the tested empirical potentials differ significantly from those predicted by both reference DFT methods, due to the very different energies of the isolated gas phase atom. In the case of GAP-17, the small offset between the LDA reference and the model prediction is the result of the isolated atom not being included in the training dataset. When using the formation energy of graphite as a reference state however, (fig. 4(b)) this offset is removed and the agreement between the empirical models and DFT improves considerably. When using both the gas phase atom and graphite as a reference, there is an excellent agreement between GAP-20 and the optB88-vdW DFT reference for all of the phases considered here.

GAP-20 uniformly predicts the atomisation energies of the tested allotropes to within an error of 1%, including the relatively subtle difference in energetics between normal cubic and hexagonal diamond and the energetics of nanotubes and fullerenes. The inclusion of the gas-phase atom in the training is vital to accurately predict these atomisation energies. There is surprisingly little difference between the formation energies predicted by the different many-body potentials tested here, though there are a few points of note. Firstly, due to their short cutoffs, the Tersoff and REBO-II potentials do not distinguish between graphite and graphene as the thermodynamically stable phase and as such their formation energies are predicted to be equal. Similarly, only the GAP-20, LCBOP and AIREBO models correctly favour cubic over hexagonal diamond, although the AIREBO model overestimates the difference in energy by a factor of 5, while the other models considered do not distinguish between the two diamond phases. A more complete evaluation of the formation energies for different chiralities of nanotubes is given in the supplemental material, for GAP-20, the energy errors for a significantly wider range of structure types are also given.

In addition to the static properties of the crystalline allotropes, it is an important characteristic of any potential that it accurately model the lattice dynamics of bulk crystals, i.e. their behaviour at finite temperature. The phonon spectrum of a material is a direct probe of this which is experimentally measurable. In addition, a number of thermodynamically relevant properties, including the thermal expansion coefficient and the constant volume heat capacity of a material may be calculated directly from the phonon dispersion relation by calculation of the free energy. It is clear therefore, why a correct prediction of the phonon dispersion relation is a highly desirable feature of an interatomic potential.

Table 1: Lattice parameters and bond lengths of the crystalline carbon phases. In the case of fullerenes, bond lengths are given in lieu of lattice parameters. Absolute values for the lattice parameters are given, with percentage errors relative to DFT in brackets. The Tersoff and REBO-II potentials have no interaction between graphite layers for any physically reasonable lattice parameters and as such these values are omitted.

| | Lattice Parameter(s) [Å] (% Error) | | | | | |
	DFT	GAP-20	Tersoff	LCBOP	REBO-II	AIREBO
Graphite (a)	2.46	2.47 (0.4)	2.53 (2.4)	2.46 (0.4)	2.46 (0.4)	2.42 (2.0)
Graphite (c)	6.65	6.71 (0.9)	-	6.36 (4.4)	-	6.72 (1.1)
Graphene	2.46	2.46 (0.0)	2.53 (2.8)	2.46 (0.0)	2.46 (0.0)	2.42 (1.6)
Diamond	3.58	3.59 (0.3)	3.57 (0.3)	3.57 (0.3)	3.57 (0.3)	3.56 (0.6)
Hexagonal Diamond	2.52	2.53 (0.4)	2.52 (0.0)	2.52 (0.0)	2.52 (0.0)	2.52 (0.0)
Nanotube-(9, 9)	4.26	4.25 (0.2)	4.35 (2.1)	4.24 (0.5)	4.26 (0.0)	4.18 (1.9)
Nanotube-(9, 0)	2.41	2.39 (0.8)	2.53 (5.0)	2.47 (2.5)	2.47 (2.5)	2.43 (0.8)
C_{60} Fullerene	1.40	1.40 (0.0)	1.46 (4.5)	1.41 (0.7)	1.42 (1.4)	1.40 (0.0)
C_{100} Fullerene	1.39	1.39 (0.0)	1.39 (0.0)	1.39 (0.0)	1.39 (0.0)	1.39 (0.0)
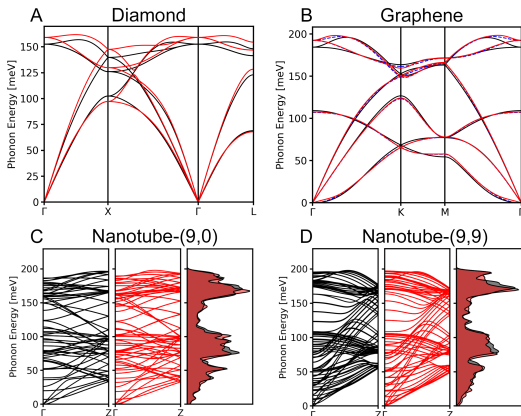
Figure 5: A. Phonon dispersion relation for diamond as predicted by GAP-20 (black) with comparison to DFT (optB88-vdW) reference data (red). B. Graphene phonon dispersion relation comparing GAP-20 and DFT (optB88-vdW) reference data. The dashed blue line shows the predicted phonon dispersion curve for the graphene-only model previously published [53] C. (9,0)-Nanotube phonon dispersion and vibrational density of states. D. (9, 9)-Nanotube phonon dispersion relation and vibrational density of states. Equivalent comparisons for the other models tested are given in the supplementary material.

Figure 5 shows the comparison between the phonon dispersion curves calculated using the reference DFT method and those calculated using the carbon GAP model for graphene, diamond, a zig-zag (9, 9) and an armchair (9, 0) carbon nanotube. Phonon dispersion curves were computed using the finite displacement method as implemented in the Phonopy Python package [95]. Equivalent curves for the other models tested are provided in the supplementary material.

We have previously reported results comparing the phonon dispersion relation for a purely graphene GAP

model, to those from experimental x-ray scattering data and a number of reference DFT methods [53]. It is useful to make a comparison between the highly targeted model previously published and the much more general GAP-20 introduced here. A particular concern might be that significantly expanding the configurational space on which we wish to train, as we have done here, would necessarily damage the quality of the predictions for graphene compared to the previous model – particularly for a property as sensitive as the phonon dispersion curves. It is demonstrated in figure 5(b) that this is not the case; the dispersion relation of the phonon curves for graphene from GAP-20 are comparable to those of the previously published graphene GAP model [53]. The energies of the phonon bands are correctly predicted across all of the high symmetry directions plotted, while the frequencies (in particular at the high symmetry points) are found to be correct to within 4 meV, which may be compared to a value of 1 meV for the pristine graphene model [53]. The quality of the GAP-20 model prediction is comparable for diamond (which cannot be modelled at all with the pristine graphene model), though with marginally larger errors for the prediction of the energies of certain bands, up to 7 meV for the higher frequency modes. GAP-20 also captures the difference in vibrational behaviour between armchair and zig-zag nanotubes remarkably well. There are some differences in the energy of certain splittings for some bands, but the magnitude of these errors is small, typically on the order of a 2-3 meV. In particular, it can be seen from fig. 5 that the vibrational density of states for the two nanotube systems agrees well with the DFT reference.

5 Surfaces of Carbon

From the point of view of atomistic simulation, surfaces present a major challenge, as their correct description requires a treatment of a number of competing physical

Table 2: Surface energies of low Miller index surfaces for common carbon allotropes. Reference energies are calculated using DFT, absolute values from each model are given, with their percentage error in brackets. Note that for the amorphous surfaces, the surface energy is averaged over a large number of different surfaces. In the amorphous case, the error provided is the average of the individual point-wise errors, rather than the error between the average surface energies.

| | Surface Energy [eV Å^{-2}] (% Error) | | | | | |
	DFT	GAP-20	Tersoff	LCBOP	REBO-II	AIREBO
Diamond (100) (As cut)	0.56	0.60 (7)	0.47 (16)	0.61 (9)	0.69 (23)	0.73 (30)
Diamond (100) (Relaxed)	0.54	0.56 (4)	0.42 (22)	0.59 (9)	0.69 (28)	0.72 (33)
Diamond (111) (As cut)	0.64	0.73 (14)	0.88 (38)	1.07 (67)	1.00 (56)	1.03 (61)
Diamond (111) (Relaxed)	0.62	0.66 (6)	0.88 (42)	1.07 (73)	1.00 (61)	1.03 (66)
Diamond (110) (As cut)	0.68	0.70 (3)	0.70 (3)	0.89 (31)	0.74 (9)	0.74 (9)
Diamond (110) (Relaxed)	0.68	0.67 (1)	0.63 (7)	0.83 (22)	0.69 (1)	0.69 (1)
Graphite (0001) (As Cut)	0.015	0.013 (13)	0 (100)	0.005 (67)	0 (100)	0.011 (27)
Graphite (0001) (Relaxed)	0.015	0.012 (20)	0 (100)	0.005 (67)	0 (100)	0.011 (27)
Amorphous Surfaces (As Cut)	0.26	0.27 (4)	0.25 (4)	0.25 (4)	0.25 (4)	0.25 (4)

interactions [81–84, 96].

We compute the surface energy for each model by first optimising the bulk structure for the parent crystal until the total energy is converged to 10^{-3} eV. We then cut the surface along the desired direction and compute the specific surface energy γ_s at T = 0 K as,

$$\gamma_\text{s} = (\text{E}_n - n\text{E}_\text{bulk})/2A, \qquad (3)$$

where E_n is the energy of the n slab layer containing two surfaces, which may be as-cut (unrelaxed) or allowed to relax and E_bulk is the energy of a single atom in the bulk structure and A is the area of the surface structure. In the case of the amorphous surfaces, due to the extent of the surface relaxation observed, we report only the as-cut surface energies.

Graphite may be readily cleaved to expose its (0001) surface, which is remarkably stable and is by far the predominant face of graphite, while in diamond, the (100), (111) and (110) surfaces are of particular interest [97]. We also compute the as-cut surface energies for an ensemble of amorphous structures, by cutting bulk amorphous systems along different directions.

The energies of several important surface cuts and their reconstructions are given in Table 2. GAP-20 typically predicts the diamond surface energies correctly to within 7 %, the exception being the case of the relaxed diamond (111) surface, where the error is slightly larger at 15 %. The structures of the relaxed surfaces were also found to be in excellent agreement, with the average error in the positions of individual surface atoms being 10^{-3} Å. The graphite (0001) surface energy is extremely small and it thus proved challenging to produce a model which could correctly characterise this, however, GAP-20 predicts the unrelaxed and relaxed surface energies correctly to within an error of 3 meV Å^{-2} (20 %). With the inclusion of vdW

interactions considered in their construction, the LCBOP and AIREBO potentials both predict the graphite (0001) surface energy rather well, with errors of 67 and 27 % respectively.

While GAP-20 achieves low errors for the surface energies of all the diamond surfaces considered, the other models generally perform well for at least one diamond surface, though none exhibit uniformly low errors. The Tersoff, REBO-II and AIREBO models predict the energies of the diamond (110) surfaces to within 10 % of the reference value. Conversely, of the empirical models only the LCBOP potential correctly predicts the energy of the diamond (100) surface; errors for the Tersoff, REBO-II and AIREBO potentials were 22, 28 and 33% respectively. None of the empirical potentials performed well for the (111) surface of diamond. The Tersoff and REBO-II models do not show any binding between graphitic layers for any reasonable initial geometry. This would lead to the spontaneous exfoliation of graphite layers and the eventual disintegration of graphite crystals in simulations employing these models.

6 Defective Carbon

A certain concentration of defects is a guarantee in any experimental material sample. Such imperfections may have a strong impact on the structural, optical and thermal properties of a material and may be introduced into a crystal structure to induce or modify properties. The engineering of defects is of great technological importance and consequently their accurate modelling by an interatomic potential is highly desirable. The possibility of re-hybridisation, which allows carbon atoms to reconstruct with differing numbers of bonds to stabilise particular structures allows carbon to have a wider variety of de-

fects than most other elements.

To the best of our knowledge, there is not a set of defect formation energies for a wide range of carbon defects computed at precisely the same level of theory. Therefore, we here assemble such a reference set, for which we compute defect formation energies in large supercells to avoid defect self-interaction in the computation of energies. For graphite, a $(6 \times 6 \times 2)$ supercell with 288 atoms and four graphite layers was used [77, 98]. In the case of graphene, a (10×10) supercell with 200 atoms was employed and for diamond a $(3 \times 3 \times 3)$ supercell with 216 atoms was used [53, 78]. Defect formation energies are calculated for the representative $(9, 9)$ and $(9, 0)$ index carbon nanotubes, which had 174 and 180 atoms in the supercells used respectively [79]. For each structure, the lattice parameters and ionic positions of the pristine structures were optimised as discussed previously. The ionic positions of the defective structures were then optimised until the energy was converged to within 10^{-5} eV, while keeping the lattice parameters fixed. We compute the formation energy E_f of a vacancy defect relative to the energy of an atom in an ideal parent structure:

$$E_f = E_d - (nE_{at} + E_{bulk}) \qquad (4)$$

Where E_d is the energy of the defective supercell structure, E_{bulk} is the energy of the undefective bulk structure and E_{at} is the energy of a single atom in the bulk structure, while n is the number of carbon atoms added (positive n) or removed (negative n) to form the defect.

The simplest of defects involves the absence of one or two atoms from their regular position in the lattice, forming monovacancy and divacancy defects. Monovacancy defects often result in unsaturated bonds at the defect site, while divacancy structures, particularly in sp^2 hybridised systems, can reconstruct to produce saturated configurations. In graphene, graphite and carbon nanotubes, the 14-membered ring formed by the removal of two adjacent atoms from the structure reconstructs to form a saturated sp^2 structure with two 5-membered and one 8-membered ring - a more stable structure known as a 5-8-5 divacancy. In graphene, this defect may further reconstruct to remove the unfavourable 8-membered ring to form a 555-777 or 5555-6-7777 divacancy reconstruction. Monovacancy coalescence is also observed in diamond, whereupon annealing at high temperature, monovacancies migrate to form divacancy defects, with fewer unsaturated bonds per absent carbon atom.
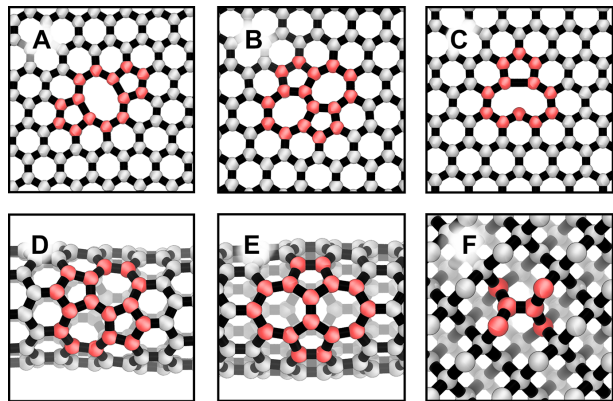

Figure 6: Images of selected carbon defect structures, with atoms in the immediate vicinity of the defect highlighted in red. (a) graphene divacancy defect (b) graphene Stone-Wales defect (c) graphene monovacancy (d) $(9, 9)$-nanotube Stone-Wales defect (transverse orientation) (e) $(9, 9)$-nanotube Stone-Wales defect (parallel orientation) (f) diamond split interstitial defect

Graphite is the only allotrope of carbon in which true interstitial defects are known, wherein interstitial atoms may be found between graphite layers [77]. The most stable arrangement of this is in a 'dumbbell' configuration, where the adatom displaces an atom in the graphite structure to form a symmetric arrangement of trigonally bonded carbon atoms above and below the sheet. Isolated interstitial atoms are not known either experimentally or from theory to be stable in diamond, rather a split interstitial is found, where a lattice site is shared by two carbon atoms which are displaced along the [100] and [$\bar{1}$00] directions [99].

In sp^2 bonded allotropes of carbon, the rotation of a single C-C bond transforms four 6-membered rings into a cluster of two 7-membered and two 5-membered rings, forming a Stone-Wales type defect [100, 101, 101, 102].

Table 3 compares the energies of a number of defects as computed with DFT, GAP-20 and the other models considered. In most cases, GAP-20 correctly predicts the defect formation energy to within an error of 10%. Typically, the prediction of the formation energies of Stone-Wales type defects was found to be extremely accurate, with no error (to within the precision of the values given) in either the graphite or graphene cases and only small errors for nanotubes. The errors for the formation energies of diamond defects tend to be larger, ranging from 25-35%, while those for defective nanotubes range from 0-11%. Anecdotally, we note that although relevant training data for the defects considered are represented in the training data, it proved challenging to achieve defect formation energies which were universally accurate. In particular this is due to the sensitivity of the formation energies to aspects such as the SOAP descriptor cutoff, specific training data included and the number of sparse points used in the training.

Table 3: Formation energies of common defects in carbon structures for GAP-20 and the other models considered, with DFT (optB88-vdW) values given as reference. Data are given in eV, with percentage errors relative to DFT given in brackets. In each case, the value given is for the optimal geometry of the defect found with that particular model.

	Formation Energy [eV] (% Error)					
	DFT	GAP-20	Tersoff	LCBOP	REBO-II	AIREBO
Graphene Stone-Wales	4.9	4.8 (2)	1.9 (61)	4.5 (8)	5.3 (8)	5.4 (10)
Graphene Monovacancy	7.7	7.0 (8)	2.5 (68)	6.9 (10)	7.5 (3)	7.2 (6)
Graphene Divacancy (5-8-5)	7.4	7.9 (7)	5.1 (31)	7.5 (1)	7.5 (1)	9.2 (24)
Graphene Divacancy (555-777)	6.6	6.9 (5)	5.2 (21)	6.6 (0)	6.8 (3)	8.7 (32)
Graphene Divacancy (5555-6-7777)	6.9	7.4 (7)	7.9 (14)	7.2 (4)	7.6 (10)	9.5 (38)
Graphene Adatom	6.4	5.9 (8)	6.7 (5)	6.8 (6)	7.4 (16)	7.8 (22)
Graphite Monovacancy	7.8	7.3 (6)	7.1 (9)	7.8 (0)	7.9 (1)	7.6 (3)
Graphite Divacancy (5-8-5)	9.6	9.2 (4)	12.6 (31)	8.2 (15)	8.0 (17)	9.7 (1)
Graphite Stone-Wales	5.4	5.6 (4)	12.8 (137)	5.7 (6)	6.0 (11)	6.0 (11)
Graphite Interstitial	7.4	7.9 (7)	9.7 (31)	7.2 (3)	7.1 (4)	6.8 (8)
Diamond Monovacancy	6.6	4.3 (35)	5.2 (36)	7.2 (11)	7.1 (4)	6.8 (8)
Diamond Divacancy	9.1	6.6 (27)	5.1 (44)	10.6 (16)	10.7 (18)	10.1 (16)
Diamond Split Interstitial	11.4	8.3 (27)	12.4 (9)	9.8 (14)	11.0 (4)	11.4 (0)
Nanotube-(9, 9) Monovacancy	6.4	5.8 (9)	-5.1 (180)	3.8 (41)	-1.6 (125)	-2.5 (139)
Nanotube-(9, 9) Divacancy	4.7	4.8 (2)	-5.5 (217)	2.9 (38)	-0.9 (119)	-2.3 (149)
Nanotube-(9, 9) Stone-Wales (Parallel)	4.4	4.5 (2)	-4.5 (202)	2.1 (52)	-2.1 (148)	-3.9 (189)
Nanotube-(9, 9) Stone-Wales (Transverse)	3.5	3.5 (0)	-5.8 (261)	2.0 (44)	-3.3 (192)	-2.00 (156)
Nanotube-(9, 0) Monovacancy	5.3	4.9 (8)	-0.9 (117)	4.4 (17)	4.7 (11)	3.4 (36)
Nanotube-(9, 0) Divacancy	3.6	3.5 (3)	-1.0 (128)	3.0 (17)	4.1 (14)	2.8 (22)
Nanotube-(9, 0) Stone-Wales (Parallel)	2.7	3.1 (15)	-1.3 (148)	3.2 (19)	3.4 (26)	3.6 (33)
Nanotube-(9, 0) Stone-Wales (Transverse)	3.5	3.2 (9)	-1.1 (131)	3.1 (11)	4.2 (20)	2.6 (26)

Considering the empirical potentials, we find that the modifications to the Tersoff potential included in the REBO-II model dramatically improve the quality of the predicted defect formation energies; percentage errors are often decreased by an order of magnitude or more when comparing these two potentials. Surprisingly, these results show that the inclusion of the long-range Lennard-Jones term in the AIREBO model often has a negative impact on the accuracy of its predicted defect formation energies, indicating that the addition of a long-range term without reparameterisation of the short-range components has adversely impacted the energetics of the model. Indeed, in the case of LCBOP, where this reparameterisation of the short range bond-order potential has been performed, we find that the errors are significantly reduced, and are in many cases comparable with the performance of GAP-20. The exception to this being the case of defective nanotubes, where LCBOP exhibits errors ranging from 11-52%. In fact, the prediction of nanotube defect formation energies proved challenging for all of the empirical models considered. In a number of cases, defect formation was found to be an energetically favourable process and was associated with a strong relaxation of the nanotube structure after defects were induced.

As well as accurately predicting the energetic cost of inducing defects in carbon structures, GAP-20 was also found to accurately predict the structures of these defects. We quantify this accuracy by calculating the structural similarity between the defect structures optimised with our GAP model and those from DFT, in the form of the root mean squared error (RMSE) between the two optimally overlapped structures. In all but a handful of cases, the RMSE for these defects is vanishingly small, with atoms having an error in their position of less than 10^{-2} Å, when comparing identical atoms from GAP-20 and DFT structures. In particular, the presence and height of the characteristic buckling of the Stone-Wales defect in graphene was well described, as was the structural distortion resulting from the presence of defects in both (9,9) and (9,0) index carbon nanotubes. Similarly, the rehybridisation and reconstruction of (5-8-5), (555-777) and (5555-6-7777) graphene divacancy defects was accurately reproduced, as were the geometries of all of the diamond defects considered. Situations in which GAP-20 showed structural inaccuracies were the nanotube monovacancy structures and the parallel Stone-Wales defect in the (9,9) index nanotube, for which the GAP model predicted a

larger distortion of the bulk nanotube structure due to the presence of the defects. We also find, that as with all the models considered here, GAP-20 does not correctly describe the asymmetry introduced through a Jahn-Teller distortion of the graphene monovacancy defect – instead predicting the monovacancy to have a symmetric geometry. This is perhaps unsurprising as the energy difference between the symmetric and asymmetric geometries is typically small (ca 350 meV). However, even in the cases illustrated here the typical error in the position of any atom was found to be only 0.1 Å. That GAP-20 is capable of accurately modelling both the energetics and structural characteristics of a wide range of carbon defects indicates its potential usefulness in a wide range of simulations in which defective structures may be relevant, including fracture, atom bombardment and simulations of membrane characteristics.

7 Liquid Carbon

As discussed previously, the requirements of a potential for the satisfactory modelling of crystalline and liquid or amorphous phases are significantly different. In the case of crystalline materials, a highly accurate description close to a local minimum for a system is required [53]. Conversely, in a liquid simulation, a vastly greater number of local configurations are explored, requiring a high degree of flexibility and transferability [62]. As in the case of GAP-17, we therefore use the liquid as a benchmark for the flexibility of our potential [62], scanning over a wide range of densities and (here) temperatures. The aim is to diagnose any possible issues which might be exposed by visiting a very diverse set of configurations during the simulations. There is a strong precedent for the study of high temperature liquids, including carbon, using DFT [103, 104]. A good agreement with DFT-MD data is therefore strong evidence for the usefulness of the potential for further studies of liquid carbon, which is present only under extreme conditions, but is nonetheless vitally important, e.g. for understanding the nucleation and formation of diamond and graphite under a wide range of circumstances [105–108].

The radial distribution function (RDF) of a liquid represents a convenient measure of its local structuring, as does its angular distribution function (ADF). Here, we compare the results of constant volume *ab initio* molecular dynamics simulations to those of GAP-20. We perform two sets of simulations, one for a range of densities between $1.5-3.5\,\mathrm{g\,cm^{-3}}$ at 5000 K and the other for a range of temperatures between 5000 - 9500 K at a fixed density of 2.5 g cm^{-3}. These simulations were performed for 216 atom systems using a chain of 5 Nosé-Hoover thermostats. *Ab initio* trajectories were generated using VASP, simulations were performed at the gamma point and data were collected for 5 ps at each temperature and pressure [71–73]. We find that there is a very good agreement between the *ab initio* data and the GAP-20 predictions for both the RDF and ADF across the wide range of temperatures studied (see figure 7). GAP-20 correctly models the increased structuring of the liquid carbon as the temperature is reduced from 9500-4500 K. At temperatures below approximately 3500 K, the GAP model predicts the liquid to form an amorphous glass which slowly graphitises (which is entirely expected because the temperature is now below the melting line). While a full discussion on the mechanism of formation and resulting morphology of graphitised amorphous carbons generated using GAP-20 is beyond the scope of the current work, this process has previously been shown to be an excellent method of differentiation between the numerous available carbon potentials [36, 37]. Figure 8 shows the RDF and ADF computed with both GAP-20 and optB88-vdW across a wide range of densities, from 1.5 to $3.5\,\mathrm{g\,cm^{-3}}$ at 5000 K. This test is particularly important as it represents dynamical simulations of structures from highly sp^1 and sp^2 hybridised (low density) through to a predominantly sp^3 hybridised liquid at higher density. GAP-20 captures this change in the bonding characteristics of liquid carbon, in particular the increase in the sp^1 hybridised fraction of the liquid at very low densities (reflected in bond angles close to 180 degrees), qualitatively similar to GAP-17 [62].
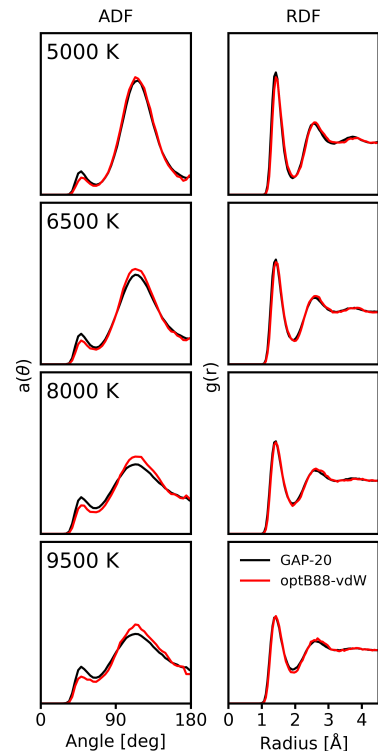

Figure 7: Angular and radial distribution functions for liquid carbon at a fixed density of 2.5 g cm^{-3} for temperatures between 5000 - 9500 K. GAP-20 results are shown in black, while reference DFT (optB88-vdW) data are given in red.

That GAP-20 can model the atomistic structure of liquid carbon at a wide variety of temperatures and densities, while maintaining the ability to accurately predict properties such as the phonon relation and defect formation energies is a reflection of the flexibility of the GAP methodology. Such wildly different systems explore a range of characteristic energies, where important fluctuations cover many orders of magnitude; in carbon, this can be anywhere from the meV range in the case of differences between graphite defect energies to fluctuations on the order of tens of electron volts as encountered in the liquid. Despite these very different energy ranges, it is not unlikely that a potential may encounter all of them over the course of a single simulation (for example during the crystallisation of a solid phase directly from the liquid) and it is therefore important that they be handled correctly.
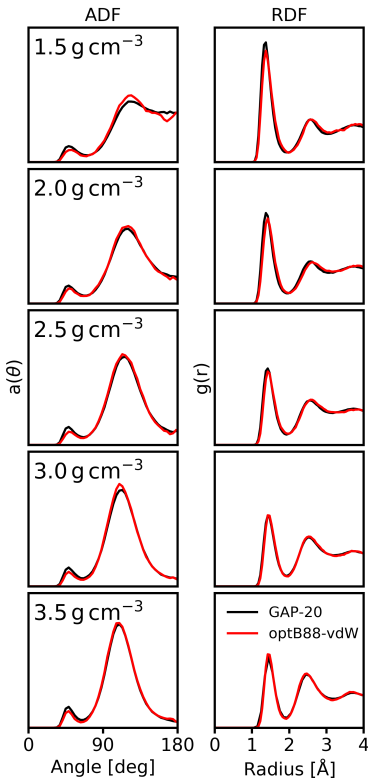

Figure 8: Angular and radial distribution functions for liquid carbon at 5000 K for a range of densities from 1.5 to 3.5 g cm^{-3}. GAP-20 results are shown in black, while reference DFT (optB88-vdW) data are given in red.

8   Transferability of the Potential

Ultimately, the purpose of any interatomic potential is that it may be used for the discovery of new and interesting phenomena. Consequently,in its application it may encounter structures which were not explicitly considered in its construction, in this case meaning that it must model structures which were not included in the training data base. It has therefore been a criticism of ML potentials that their poor performance in extrapolation might inhibit their use for scientific discovery. As discussed earlier, the problem of extrapolation is circumvented by the fact that we consider only the local environment around a particular atom to be important for predicting its atomic energy and the forces acting upon it. While the problem of exploring the entirety of the 3N dimensional chemical space is indeed intractable, sufficiently sampling all of the physically relevant local environments is not [59].

We demonstrate this here by performing a diagnostic GAP driven random structure search (GAP-RSS), similar in spirit to Refs. [109] and [5], and demonstrate that the predicted energies of these structures agree well with those from DFT [5, 60, 85]. We then calculate a number of high energy pathways for specific transformations not included in the training and compare these to DFT. Both of these tests serve the purpose of exploring the high energy regions of the potential energy surface which may be explored during molecular dynamics simulations or geometry optimisation and which must be well described for an ML model to be transferable. Importantly, they are both explicitly designed to include configurations which are not present in the training data set of GAP-20.

To perform the first test, we generate a cubic unit cell with lattice parameter a = 3 Å. In this cell, we randomly place 8 carbon atoms, avoiding any overlaps such that the distance between any two carbon atoms is not less than 2 Å. This process is performed to generate 1000 initial randomised geometries. The LAMMPS package is then used to optimise lattice vectors of the cell independently using conjugate gradient descent, while maintaining their orthogonality, until the total energy is converged to within 10^{-8} eV [110]. Following this, the positions of the atoms in the unit cell are optimised using a FIRE algorithm [111], until the total energy is again converged to within 10^{-8} eV. This cycle is repeated twice more before performing a final conjugate gradient optimisation of the atomic positions and cell vectors until the total energy is converged to 10^{-10} eV.
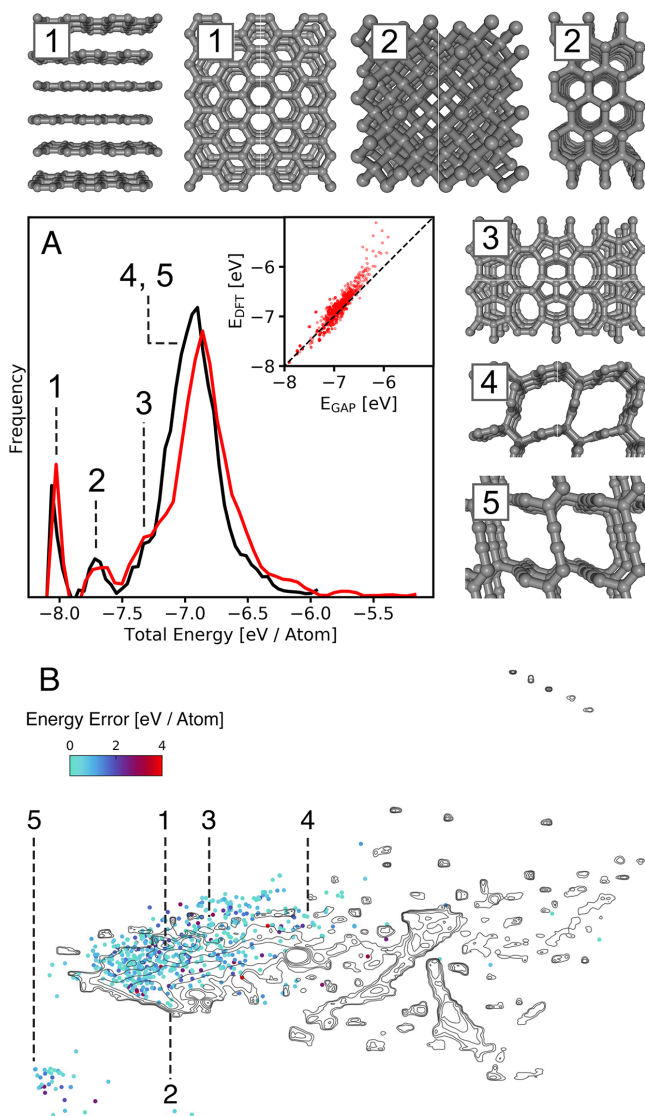
Figure 9: (a) A comparison of the histograms of energies of structures identified by GAP-RSS, given in eV / atom, showing good agreement for the prediction of the energy of structures between GAP-20 (shown in black) and DFT (optB88-vdW) (shown in red). A number of examples of structures identified in GAP-20 driven random structure search are shown. The position of each of the example structures on the histogram is indicated by their numbering, 1) AB stacked graphite, AA stacked graphite. 2) cubic and hexagonal diamond. 3) Haekelite 4) crosslinked graphitic structure. 5) Novel carbon structure with high proportion of sp^1 hybridised carbon atoms (b) The structures resulting from the GAP-RSS projected into the sketch-map representation from Fig 1. The density of the structures present in the training data are indicated by the contour lines, while the structures identified from the GAP-RSS are shown as individual points.

To validate the results of our GAP-RSS, we recompute the energies of the structures found using the ref-

erence DFT method used to train the model. We note that for across all 1000 structures, the predicted energy agrees well with the energy predicted from DFT. It has previously been shown that correctly identifying low energy structures from a RSS is an extremely challenging task for empirical models, which often predict qualitatively incorrect behaviour and fail to find physically relevant configurations due to their having many more local minima than the DFT PES [112, 113].

Our GAP-RSS correctly identifies a range of important low-energy carbon allotropes, as well as numerous more exotic species. In particular, AB-stacked graphite was found as the lowest energy allotrope of carbon. AA- and ABC- stacked graphite allotropes are also identified in the search, their energy is correctly predicted to be higher than that of the AB stacked graphite structure. Furthermore, both diamond and lonsdaleite are both correctly identified. We also identify a number of more exotic carbon allotropes, some of which are known either from experiment or theory but were not included in the training dataseset, including crosslinked graphite structures, porous carbon cages and a variety of haekelite structures. For the vast majority of structures found during the GAP-20 driven random structure search, the predicted energies from both DFT and GAP-20 agree well (figure 9).

We also return at this stage to the sketch-map representation of the training dataset given in figure 1. In figure 9(b) we provide a projection of the GAP-RSS structures onto this sketch-map representation. GAP-RSS points are coloured according to the GAP-20 energy error. The density of structures present in the original training dataset is indicated by black contour lines. It is clear that most structures found are clustered in the region representing the bulk amorphous and crystalline polymorphs, with very few structures representative of fullerenes or nanotubes identified. This is a reflection of the fact that only 8 atoms are included in the unit cell used for the RSS. Additionally, the RSS procedure employed begins with simulation cells which are fully periodic and with no symmetry constraints imposed on the initial atomic positions. In the lower left of the sketch-map is a cluster which is structurally distinct from those present in the training data, as indicated by its large separation from other points in the sketch-map. These structures are characterised by their highly sp^1 rich character. Although a significant number of amorphous structures which are rich in sp^1 hybridised carbon atoms are included in the training data, there are indeed very few crystalline sp^1 rich structures. Despite being structurally distinct from anything included in the training dataset, the error in the GAP-20 prediction for the energy of these structures remains low. This indicates excellent performance for GAP-20 in applications where transferability to potentially novel structures is important.
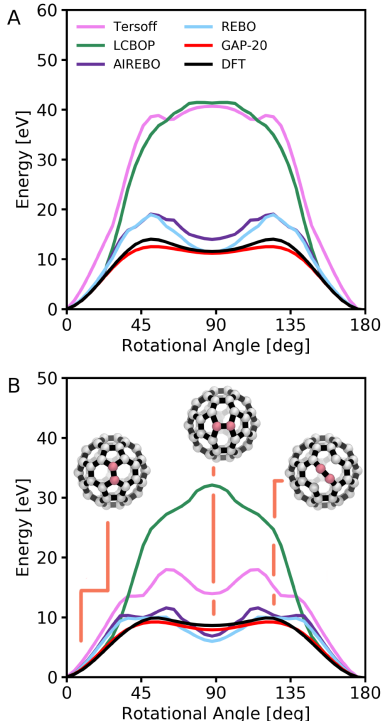
Figure 10: Energies for rigid transformations of a C-C bond in graphene (a) and in a C60 fullerene (b). Results from GAP-20, DFT (optB88-vdW) and a selection of empirical potentials are shown.

We also test GAP-20 on a number of specific structural transformations. Although our GAP model is not trained explicitly on reaction barriers, it is useful to test how well the model performs for the prediction of the types of barriers which might be encountered in studies of the reactivity of carbon nanostructures. To this end, we compare the predictions of our GAP model to those of DFT for two approximate transformations; a rigid bond rotation in graphene and a C60 fullerene. Since these calculations are performed on rigid structures, rather than for example using nudged elastic band calculations, the barriers calculated here will not be true defect formation barriers. They are, however, still representations of physically reasonable points on the potential energy surface which are not included in the training dataset and so form a useful test of the potential compared to other models [66, 114].

Figure 10 (a) shows the barrier to rigid rotation of a C-C bond within a graphene sheet as predicted by GAP-20, and the tested empirical potentials. The performance of GAP-20 on this test is reassuring for its wider application, it achieves excellent accuracy with respect to both the height of the local minimum in the rotation and the height of the barrier. The AIREBO and REBO potentials capture the general shape and height of the barrier, but predict jagged curves for the rotation, as compared to the smooth variation from DFT. The LCBOP and Tersoff po-

tentials perform poorly, overestimating the energy of the rotation by more than 30 eV, and erroneously situating a maximum in the potential energy where a minimum is found from DFT. In the case of the Tersoff potential, two additional spurious minima are located close to where the DFT maxima are located.

A similar situation is observed for the behaviour of the C60 rotational barrier in figure 10 (b). Here, it is again seen that GAP-20 performs well, providing a good estimation of the barrier height and shape with respect to DFT. The REBO, AIREBO and Tersoff potentials all situate spurious minima in the potential energy close to where the maxima in the reference DFT curve are located, although they do also predict a minimum at the correct rotation. LCBOP again overestimates the energy of the barrier by 20 eV, and situates a maximum in the potential energy surface where a minimum ought to be located.

9   Conclusion

The advantages conferred by the flexibility of the Gaussian approximation potential framework are made clear by the wide variety of structures which are accurately treated by GAP-20. The variable hybridisation of carbon makes it an extremely challenging element to model using empirical potentials; its structurally diverse allotropes are energetically similar and the properties of these depend on an broad range of physical interactions, from the weak van der Waals forces binding graphite to the stiff covalent bonds of diamond. We have demonstrated here a model which is equally suited to modelling not just these two bulk structures, but defects, surfaces and liquid carbon as well. Wherever possible, we have validated the performance of GAP-20 against the reference DFT method and shown it to perform well for a number of physical properties across the different phases. Included in these are a number of processes involving bond breaking and formation, some of which have been challenging for cheaper empirical potentials by construction. Tests for transferability, specifically by diagnostic GAP-RSS runs and the study of transformations not included in the training, suggest that GAP-20 could readily be applied to more thorough explorations of the carbon potential energy landscape, for example, in the search for larger fullerenes [61, 115] or in crystal-structure prediction by expanding on Refs. [5] and [109]. Further applications may include the more detailed study of non-graphitising or "hard" carbons [116–119], following on from earlier GAP-17 based studies in Ref. [57] and [58].

Despite the many potential applications of GAP-20, the model is not without its shortcomings. While it remains significantly more computationally affordable than direct *ab initio* simulation (in particular for large systems) the cost of its evaluation is much greater than that of empirical potentials (Supplementary Fig. 12), and therefore the latter will still give access to even larger-scale systems

[36]. We also note that 'real' carbon is rarely found in isolation – hydrogenation and oxidation of carbon structures is not considered here. The expansion of the scope of the potential to treat hydrogenated or oxidised structures would complicate the process of training both by requiring a larger training dataset and by requiring the inclusion of a number of interactions not considered here. In addition to long ranged van der Waals interactions (which are only considered approximately in the current work), the introduction of other elements introduces the associated complexities of substantial charge rearrangements: polar bonds and partial charges. Long ranged Coulomb interactions, dipole-dipole and higher order multipole interactions remain a challenge for ML potentials. We note that the combination of pure carbon simulations (using GAP-17) and subsequent density-functional analyses of hydrogenation and oxidation [36] or metal intercalation [58] has proven fruitful, and we expect that further studies of this type will be facilitated by GAP-20, particularly when low-density, dispersion-dominated nanostructures are concerned.

We believe that we have achieved an excellent compromise for our potential, in that it accurately models the wide range of structures required to make it broadly applicable. We do not claim perfect accuracy for all properties, however; we accept that fitting to such a wide range of structures will necessarily impact the accuracy in some areas. Notably, a large number of structures which were generated as part of the total training dataset are excluded from the final training. Conversely, many have been included which might be irrelevant for a researcher's intended purpose. With this in mind, we have made freely available the total training dataset (structures, energies, forces and virial coefficients) produced as part of this work. While we do not believe that this will typically be necessary, it is a further virtue of the GAP framework that a potential may be readily retrained to suit a particular purpose simply by modifying the composition of the training configurations used, we believe it is beneficial to offer the opportunity for users to tune the model to target higher accuracy in a particular region of interest.

In addition to the training dataset, the potential introduced here is provided in the form of an XML file and has been made freely available, along with the GAP code at `http://www.libatoms.org`, it has the unique identifier GAP_2020_4_27_60_2_50_5_436 and may be used within the QUIP software package which can be found at `https://github.com/libAtoms/QUIP`. GAP-20 may be used for simulations directly in LAMMPS, using the QUIP for LAMMPS plugin [110].

10 Supplementary Material

See [Supplementary Material] for full details of computed formation energies and phonon dispersion curves for all models, further information on GAP hyper-parameter se-lection and command line argument used, graphene bilayer separation curves and force errors for various configurations. More information on the optimisation and computational cost of GAP-20 compared to DFT is also given.

11 Acknowledgements

12 Data Availability

The data that support the findings of this study are openly available at `http://www.libatoms.org/Home/DataRepository` and on request from the authors.

References

[1] K. S. Novoselov, A. K. Geim, S. V. Morozov, D. Jiang, Y. Zhang, S. V. Dubonos, I. V. Griegorieva, and A. A. Firsov, "Electric Field Effect in Atomically Thin Carbon Films," *Science*, vol. 306, no. 5696, pp. 666–669, 2004.

[2] H. Kroto, J. Heath, S. O'Brien, R. Curl, and R. E. Smalley, "C60: Buckminsterfullerene," *Nature*, vol. 318, pp. 162–163, 1985.

[3] M. Martinez-Canales and C. J. Pickard, "Thermodynamically Stable Phases of Carbon at Multiterapascal Pressures," *Physical Review Letters*, vol. 108, no. 4, p. 045704, 2012.

[4] R. C. Powles, N. A. Marks, and D. W. M. Lau, "Self-assembly of sp2 -bonded carbon nanostructures from amorphous precursors," *Physical Review B - Condensed Matter and Materials Physics*, vol. 79, no. 7, pp. 1–11, 2009.

[5] V. L. Deringer, G. Csányi, and D. M. Proserpio, "Extracting Crystal Chemistry from Amorphous Carbon Structures," *ChemPhysChem*, vol. 18, no. 8, pp. 873–877, 2017.

[6] D. Tománek, *Guide Through the Nanocarbon Jungle*. San Rafael: Morgan & Claypool Publishers, 1 ed., 2014.

[7] R. Mirzayev, K. Mustonen, M. R. A. Monazam, A. Mittelberger, T. J. Pennycook, C. Mangler, T. Susi, J. Kotakoski, and J. C. Meyer, "Buckyball sandwiches," *Science Advances*, vol. 3, no. 6, p. e1700176, 2017.

[8] C. Lee, X. Wei, J. W. Kysar, and J. Hone, "Measurement of the elastic properties and intrinsic strength of monolayer graphene.," *Science*, vol. 321, no. 5887, pp. 385–388, 2008.

[9] M. H. Nazare and A. J. Neves, *Properties Growth and Applications of Diamond*. London: INSPEC, 1 ed., 2001.

[10] A. K. Geim, "Graphene: Status and prospects," *Science*, vol. 324, no. 5934, pp. 1530–1534, 2009.

[11] P. Avouris, Z. Chen, and V. Perebeinos, "Carbon-based electronics.," *Nature Nanotechnology*, vol. 2, no. 10, pp. 605–15, 2007.

[12] Y. Yan, J. Miao, Z. Yang, F. X. Xiao, H. B. Yang, B. Liu, and Y. Yang, "Carbon nanotube catalysts: Recent advances in synthesis, characterization and applications," *Chemical Society Reviews*, vol. 44, no. 10, pp. 3295–3346, 2015.

[13] W. Zhang, S. Zhu, R. Luque, S. Han, L. Hu, and G. Xu, "Recent development of carbon electrode materials and their bioanalytical and environmental applications," *Chemical Society Reviews*, vol. 45, no. 3, pp. 715–752, 2016.

[14] Y.-n. Zhang, Q. Niu, X. Gu, N. Yang, and G. Zhao, "Recent Progress of Carbon Nanomaterials for Electrochemical Detection and Removal of Environmental Pollutants," *Nanoscale*, 2019.

[15] Z. Yang, J. Ren, Z. Zhang, X. Chen, G. Guan, L. Qiu, Y. Zhang, and H. Peng, "Recent Advancement of Nanostructured Carbon for Energy Applications," *Chemical Reviews*, vol. 115, no. 11, pp. 5159–5223, 2015.

[16] W. Yuan, Y. Zhang, L. Cheng, H. Wu, L. Zheng, and D. Zhao, "The applications of carbon nanotubes and graphene in advanced rechargeable lithium batteries," *Journal of Materials Chemistry A*, vol. 4, no. 23, pp. 8932–8951, 2016.

[17] A. S. Aricò, P. Bruce, B. Scrosati, J. M. Tarascon, and W. Van Schalkwijk, "Nanostructured materials for advanced energy conversion and storage devices," *Nature Materials*, vol. 4, no. 5, pp. 366–377, 2005.

[18] I. N. Kholmanov, C. W. Magnuson, R. Piner, J. Y. Kim, A. E. Aliev, C. Tan, T. Y. Kim, A. A. Zakhidov, G. Sberveglieri, R. H. Baughman, and R. S. Ruoff, "Optical, electrical, and electromechanical properties of hybrid graphene/carbon nanotube films," *Advanced Materials*, vol. 27, no. 19, pp. 3053–3059, 2015.

[19] F. Bonaccorso, Z. Sun, T. Hasan, and A. C. Ferrari, "Graphene Photonics and Optoelectronics," *Nature Photonics*, vol. 4, no. 9, pp. 611–622, 2010.

[20] A. H. Castro Neto, F. Guinea, N. M. R. Peres, K. S. Novoselov, and A. K. Geim, "The electronic properties of graphene," *Reviews of Modern Physics*, vol. 81, no. 1, pp. 109–162, 2009.

[21] C. Farrera, F. Torres Andón, and N. Feliu, "Carbon Nanotubes as Optical Sensors in Biomedicine," *ACS Nano*, vol. 11, no. 11, pp. 10637–10643, 2017.

[22] A. Courvoisier, M. J. Booth, and P. S. Salter, "Inscription of 3D waveguides in diamond using an ultrafast laser," *Applied Physics Letters*, vol. 109, no. 3, 2016.

[23] P. Latawiec, V. Venkataraman, M. J. Burek, B. J. M. Hausmann, I. Bulu, and M. Lončar, "On-chip diamond Raman laser," *Optica*, vol. 2, no. 11, p. 924, 2015.

[24] L. Pastewka, S. Moser, P. Gumbsch, and M. Moseler, "Anisotropic mechanical amorphization drives wear in diamond," *Nature Materials*, vol. 10, no. 1, pp. 34–38, 2011.

[25] T. B. Shiell, D. G. McCulloch, D. R. McKenzie, M. R. Field, B. Haberl, R. Boehler, B. A. Cook, C. De Tomas, I. Suarez-Martinez, N. A. Marks, and J. E. Bradby, "Graphitization of Glassy Carbon after Compression at Room Temperature," *Physical Review Letters*, vol. 120, no. 21, p. 215701, 2018.

[26] J. Tersoff, "Empirical interatomic potential for carbon, with applications to amorphous carbon," *Physical Review Letters*, vol. 61, no. 25, pp. 2879–2882, 1988.

[27] D. W. Brenner, "Empirical potential for hydrocarbons for use in simulating the chemical vapor deposition of diamond films," *Physical Review B*, vol. 42, no. 15, pp. 9458–9471, 1990.

[28] T. C. O'Connor, J. Andzelm, and M. O. Robbins, "AIREBO-M: A reactive model for hydrocarbons at extreme pressures," *Journal of Chemical Physics*, vol. 142, no. 2, p. 024903, 2015.

[29] S. J. Stuart, A. B. Tutein, and J. A. Harrison, "A reactive potential for hydrocarbons with intermolecular interactions," *The Journal of Chemical Physics*, vol. 112, no. 2000, pp. 6472–6486, 2000.

[30] J. H. Los and a. Fasolino, "Intrinsic long-range bond-order potential for carbon: Performance in Monte Carlo simulations of graphitization," *Physical Review B*, vol. 68, no. 2, p. 24107, 2003.

[31] L. M. Ghiringhelli, J. H. Los, A. Fasolino, and E. J. Meijer, "Improved long-range reactive bond-order potential for carbon. II. Molecular simulation of liquid carbon," *Physical Review B*, vol. 72, no. 21, p. 214103, 2005.

[32] J. H. Los, L. M. Ghiringhelli, E. J. Meijer, and A. Fasolino, "Improved long-range reactive bond-order potential for carbon. I. Construction (Physical Review B. Condensed Matter and Materials Physics (2005) 72 (214102))," *Physical Review B*, vol. 73, no. 22, p. 229901, 2006.

[33] N. A. Marks, "Generalizing the environment-dependent interaction potential for carbon," *Physical Review B*, vol. 63, no. December 2000, pp. 1–7, 2006.

[34] L. Pastewka, P. Pou, R. Pérez, P. Gumbsch, and M. Moseler, "Describing bond-breaking processes by reactive potentials: Importance of an environment-dependent interaction range," *Physical Review B - Condensed Matter and Materials Physics*, vol. 78, no. 16, p. 161402, 2008.

[35] S. Goverapet Srinivasan, A. C. T. Van Duin, and P. Ganesh, "Development of a ReaxFF potential for carbon condensed phases and its application to the thermal fragmentation of a large fullerene," *Journal of Physical Chemistry A*, vol. 119, no. 4, pp. 571–580, 2015.

[36] C. de Tomas, A. Aghajamali, J. L. Jones, D. J. Lim, M. J. Lopez, I. Suarez-Martinez, and N. A. Marks, "Transferability in interatomic potentials for carbon," *Carbon*, vol. 155, pp. 624–634, 2019.

[37] C. de Tomas, I. Suarez-Martinez, and N. A. Marks, "Graphitization of amorphous carbons: A comparative study of interatomic potentials," *Carbon*, vol. 109, pp. 681–693, 2016.

[38] J. Behler and M. Parrinello, "Generalized neural-network representation of high-dimensional potential-energy surfaces," *Physical Review Letters*, vol. 98, no. 14, p. 146401, 2007.

[39] A. P. Bartók, M. C. Payne, R. Kondor, and G. Csányi, "Gaussian approximation potentials: The accuracy of quantum mechanics, without the electrons," *Physical Review Letters*, vol. 104, no. 13, p. 136403, 2010.

[40] K. T. Schütt, H. E. Sauceda, P. Kindermans, A. Tkatchenko, K. Müller, H. E. Sauceda, P. Kindermans, A. Tkatchenko, and K. M, "SchNet – A deep learning architecture for molecules and materials SchNet – A deep learning architecture for molecules and materials," *Journal of Chemical Physics*, vol. 148, p. 241722, 2018.

[41] T. D. Huan, R. Batra, J. Chapman, S. Krishnan, L. Chen, and R. Ramprasad, "A universal strategy for the creation of machine learning-based atomistic force fields," *npj Computational Materials*, vol. 3, no. 1, p. 37, 2017.

[42] A. P. Bartók, S. De, C. Poelking, N. Bernstein, J. R. Kermode, G. Csányi, and M. Ceriotti, "Machine learning unifies the modeling of materials and molecules," *Science Advances*, vol. 3, p. e1701816, 2017.

[43] B. Kolb, X. Luo, X. Zhou, B. Jiang, and H. Guo, "High-Dimensional Atomistic Neural Network Potentials for Molecule-Surface Interactions: HCl Scattering from Au(111)," *Journal of Physical Chemistry Letters*, vol. 8, pp. 666–672, 2017.

[44] P. E. Dolgirev, I. A. Kruglov, and A. R. Oganov, "Machine learning scheme for fast extraction of chemically interpretable interatomic potentials," *AIP Advances*, vol. 6, p. 085318, 2016.

[45] A. Glielmo, P. Sollich, and A. De Vita, "Accurate interatomic force fields via machine learning with covariant kernels," *Physical Review B*, vol. 95, no. 21, p. 214302, 2017.

[46] V. Kůrková, "Kolmogorov's theorem and multilayer neural networks," *Neural Networks*, vol. 5, no. 3, pp. 501–506, 1992.

[47] C. M. Handley and J. Behler, "Next generation interatomic potentials for condensed systems," *The European Physical Journal B*, vol. 87, p. 152, 2014.

[48] J. Behler, "Neural network potential-energy surfaces in chemistry: A tool for large-scale simulations," *Physical Chemistry Chemical Physics*, vol. 13, no. 40, pp. 17930–17955, 2011.

[49] J. Behler, "Perspective: Machine learning potentials for atomistic simulations," *Journal of Chemical Physics*, vol. 145, no. 17, p. 170901, 2016.

[50] V. L. Deringer, M. A. Caro, and G. Csányi, "Machine Learning Interatomic Potentials as Emerging Tools for Materials Science," *Advanced Materials*, vol. 31, no. 46, p. 1902765, 2019.

[51] R. Z. Khaliullin, H. Eshet, T. D. Kühne, J. Behler, and M. Parrinello, "Graphite-diamond phase coexistence study employing a neural-network mapping of the ab initio potential energy surface," *Physical Review B*, vol. 81, no. 10, p. 100103, 2010.

[52] R. Z. Khaliullin, H. Eshet, T. D. Kühne, J. Behler, and M. Parrinello, "Nucleation mechanism for the direct graphite-to-diamond phase transition," *Nature Materials*, vol. 10, no. 9, pp. 693–697, 2011.

[53] P. Rowe, G. Csányi, D. Alfè, and A. Michaelides, "Development of a machine learning potential for graphene," *Physical Review B*, vol. 97, p. 054303, 2018.

[54] M. A. Caro, V. L. Deringer, J. Koskinen, T. Laurila, and G. Csányi, "Growth Mechanism and Origin of High sp3 Content in Tetrahedral Amorphous Carbon," *Physical Review Letters*, vol. 120, no. 16, p. 166101, 2018.

[55] V. L. Deringer, M. A. Caro, R. Jana, A. Aarva, S. R. Elliott, T. Laurila, G. Csányi, and L. Pastewka, "Computational Surface Chemistry of Tetrahedral Amorphous Carbon by Combining Machine Learning and Density Functional Theory," *Chemistry of Materials*, vol. 30, no. 21, pp. 7438–7445, 2018.

[56] M. A. Caro, A. Aarva, V. L. Deringer, G. Csányi, and T. Laurila, "Reactivity of Amorphous Carbon Surfaces: Rationalizing the Role of Structural Motifs in Functionalization Using Machine Learning," *Chemistry of Materials*, vol. 30, no. 21, pp. 7446–7455, 2018.

[57] V. L. Deringer, C. Merlet, Y. Hu, T. H. Lee, J. A. Kattirtzi, O. Pecher, G. Csányi, S. R. Elliott, and C. P. Grey, "Towards an atomistic understanding of disordered carbon electrode materials," *Chemical Communications*, vol. 54, no. 47, pp. 5988–5991, 2018.

[58] J. X. Huang, G. Csányi, J. B. Zhao, J. Cheng, and V. L. Deringer, "First-principles study of alkali-metal intercalation in disordered carbon anode materials," *Journal of Materials Chemistry A*, vol. 7, no. 32, pp. 19070–19080, 2019.

[59] A. P. Bartók, J. Kermode, and N. Bernstein, "Machine Learning a General-Purpose Interatomic Potential for Silicon," *Physical Review X*, vol. 8, no. 4, p. 41048, 2018.

[60] C. J. Pickard and R. J. Needs, "Ab initio random structure searching," *Journal of Physics: Condensed Matter*, vol. 23, p. 053201, 2011.

[61] D. Wales, *Energy Landscapes: Applications to Clusters, Biomolecules and Glasses.* Cambridge: Cambridge University Press, 1 ed., 2004.

[62] V. L. Deringer and G. Csányi, "Machine learning based interatomic potential for amorphous carbon," *Physical Review B*, vol. 95, no. 9, p. 094203, 2017.

[63] A. P. Bartók, R. Kondor, and G. Csányi, "On representing chemical environments," *Physical Review B*, vol. 87, no. 18, p. 184115, 2013.

[64] J. Behler, "Atom-centered symmetry functions for constructing high-dimensional neural network potentials," *Journal of Chemical Physics*, vol. 134, no. 7, p. 074106, 2011.

[65] P. Gasparotto, R. H. Meißner, and M. Ceriotti, "Recognizing Local and Global Structural Motifs at the Atomic Scale," *Journal of Chemical Theory and Computation*, vol. 14, pp. 486–498, 2018.

[66] D. J. Wales, "Closed-shell structures and the building game," *Chemical Physics Letters*, vol. 141, no. 6, pp. 478–484, 1987.

[67] K. Lee, É. D. Murray, L. Kong, B. I. Lundqvist, and D. C. Langreth, "Higher-accuracy van der Waals density functional," *Physical Review B - Condensed Matter and Materials Physics*, vol. 82, no. 8, p. 081101, 2010.

[68] J. Klimeš, D. R. Bowler, and A. Michaelides, "Van der Waals density functionals applied to solids," *Physical Review B*, vol. 83, no. 19, p. 195131, 2011.

[69] M. Dion, H. Rydberg, E. Schröder, D. C. Langreth, and B. I. Lundqvist, "Van der Waals density functional for general geometries," *Physical Review Letters*, vol. 92, no. 24, p. 246401, 2004.

[70] J. Klimeš, D. R. Bowler, and A. Michaelides, "Chemical accuracy for the van der Waals density functional.," *Journal of Physics: Condensed Matter*, vol. 22, no. 2, p. 022201, 2010.

[71] G. Kresse and J. Furthmüller, "Efficient iterative schemes for ab initio total-energy calculations using a plane-wave basis set," *Physical Review B*, vol. 54, no. 16, pp. 11169–11186, 1996.

[72] G. Kresse and J. Furthmüller, "Efficiency of ab-initio total energy calculations for metals and semiconductors using a plane-wave basis set," *Computational Materials Science*, vol. 6, no. 1, pp. 15–50, 1996.

[73] G. Kresse, "From ultrasoft pseudopotentials to the projector augmented-wave method," *Physical Review B*, vol. 59, no. 3, pp. 1758–1775, 1999.

[74] H. Monkhorst and J. Pack, "Special points for Brillouin zone integrations," *Physical Review B*, vol. 13, no. 12, pp. 5188–5192, 1976.

[75] G. Graziano, J. Klimeš, F. Fernandez-Alonso, and A. Michaelides, "Improved description of soft layered materials with van der Waals density functional theory," *Journal of Physics: Condensed Matter*, vol. 24, no. 42, p. 424216, 2012.

[76] R. Hoffmann, A. A. Kabanov, A. A. Golov, and D. M. Proserpio, " Homo Citans and Carbon Allotropes: For an Ethics of Citation ," *Angewandte Chemie International Edition*, vol. 55, no. 37, pp. 10962–10976, 2016.

[77] L. Li, S. Reich, and J. Robertson, "Defect energies of graphite: Density-functional calculations," *Physical Review B - Condensed Matter and Materials Physics*, vol. 72, no. 18, p. 184109, 2005.

[78] T. Xu and L. Sun, "Structural defects in graphene," *Defects in Advanced Electronic Materials and Novel Low Dimensional Structures*, vol. 5, no. 1, pp. 137–160, 2018.

[79] J. C. Charlier, "Defects in carbon nanotubes," *Accounts of Chemical Research*, vol. 35, no. 12, pp. 1063–1069, 2002.

[80] S. T. Skowron, I. V. Lebedeva, A. M. Popov, and E. Bichoutskaia, "Energetics of atomic scale structure changes in graphene," *Chemical Society Reviews*, vol. 44, no. 44, pp. 3143–3176, 2015.

[81] J. Ristein, "Diamond surfaces : familiar and amazing," *Applied Physics A*, vol. 384, pp. 377–384, 2006.

[82] G. Kern and J. Hanfer, "Ab initio molecular-dynamics studies of the graphitization of flat and stepped diamond (111) surfaces," *Physical Review B*, vol. 19, p. 13167, 1998.

[83] N. Ooi, A. Rairkar, and J. B. Adams, "Density functional study of graphite bulk and surface properties," *Carbon*, vol. 44, no. 2, pp. 231–242, 2006.

[84] G. Kern and J. Hafner, "Ab initio calculations of the atomic and electronic structure of diamond (111) surfaces with steps," *Physical Review B*, vol. 58, no. 4, pp. 2161–2169, 1998.

[85] V. L. Deringer, C. J. Pickard, and G. Csányi, "Data-Driven Learning of Total and Local Energies in Elemental Boron," *Physical Review Letters*, vol. 120, no. 15, p. 156001, 2018.

[86] S. De, A. P. Bartók, G. Csányi, and M. Ceriotti, "Comparing molecules and solids across structural and alchemical space," *Physical Chemistry Chemical Physics*, vol. 18, no. 20, p. 13754, 2016.

[87] M. Ceriotti, G. A. Tribello, and M. Parrinello, "Simplifying the representation of complex free-energy landscapes using sketch-map.," *Proceedings of the National Academy of Sciences*, vol. 108, no. 32, pp. 13023–13028, 2011.

[88] A. P. Bartók, M. J. Gillan, F. R. Manby, and G. Csányi, "Machine-learning approach for one- and two-body corrections to density functional theory: Applications to molecular and condensed water," *Physical Review B*, vol. 88, no. 5, p. 054104, 2013.

[89] D. Dragoni, T. D. Daff, G. Csanyi, and N. Marzari, "Achieving DFT accuracy with a machine-learning interatomic potential: thermomechanics and defects in bcc ferromagnetic iron," *Physical Review Materials*, vol. 2, p. 013808, 2017.

[90] S. Fujikake, V. L. Deringer, T. H. Lee, M. Krynski, S. R. Elliott, G. Csányi, S. Fujikake, V. L. Deringer, H. Lee, and M. Krynski, "Gaussian approximation potential modeling of lithium intercalation in carbon nanostructures," *Journal of Chemical Physics*, vol. 148, p. 241714, 2018.

[91] W. J. Szlachta, A. P. Bartók, and G. Csányi, "Accuracy and transferability of Gaussian approximation potential models for tungsten," *Physical Review B*, vol. 90, no. 10, p. 104018, 2014.

[92] M. J. Willatt, F. Musil, and M. Ceriotti, "Feature optimization for atomistic machine learning yields a

data-driven construction of the periodic table of the elements," *Physical Chemistry Chemical Physics*, vol. 20, no. 47, pp. 29661–29668, 2018.

[93] F. A. Faber, A. S. Christensen, B. Huang, and O. A. Von Lilienfeld, "Alchemical and structural distribution based representation for universal quantum machine learning," *Journal of Chemical Physics*, vol. 148, no. 24, 2018.

[94] A. S. Christensen, L. A. Bratholm, F. A. Faber, and O. Anatole Von Lilienfeld, "FCHL revisited: Faster and more accurate quantum machine learning," *Journal of Chemical Physics*, vol. 152, no. 4, p. 044107, 2020.

[95] A. Togo and I. Tanaka, "First principles phonon calculations in materials science," *Scripta Materialia*, vol. 108, pp. 1–5, 2015.

[96] G. Kern and J. Hafner, "Ab initio calculations of the atomic and electronic structure of clean and hydrogenated diamond (110) surfaces," *Physical Review B*, vol. 56, no. 7, pp. 4203–4210, 1997.

[97] S. Thinius, M. M. Islam, and T. Bredow, "Reconstruction of low-index graphite surfaces," *Surface Science*, vol. 649, no. 1, pp. 60–65, 2016.

[98] M. I. J. Probert and M. C. Payne, "Improving the convergence of defect calculations in supercells: An ab initio study of the neutral silicon vacancy," *Physical Review B*, vol. 67, no. 7, p. 075204, 2003.

[99] D. Hunt, D. Twitchen, M. Newton, J. Baker, and T. Anthony, "Identification of the neutral carbon (100)-split interstitial in diamond," *Physical Review B - Condensed Matter and Materials Physics*, vol. 61, no. 6, pp. 3863–3876, 2000.

[100] A. J. Stone and D. J. Wales, "Theoretical Studies of Icosahedral C60 and Some Related Species," *Chemical Physics Letters*, vol. 128, no. 5, pp. 501–503, 1986.

[101] J. Kotakoski, J. C. Meyer, S. Kurasch, D. Santos-Cottin, U. Kaiser, and A. V. Krasheninnikov, "Stone-Wales-type transformations in carbon nanostructures driven by electron irradiation," *Physical Review B - Condensed Matter and Materials Physics*, vol. 83, no. 24, p. 245420, 2011.

[102] J. Ma, D. Alfè, A. Michaelides, and E. Wang, "Stone-Wales defects in graphene and other planar sp2 -bonded materials," *Physical Review B*, vol. 80, no. 4, p. 033407, 2009.

[103] A. A. Correa, S. A. Bonev, and G. Galli, "Carbon under extreme conditions: Phase boundaries and electronic properties from first-principles theory," *Proceedings of the National Academy of Sciences of the United States of America*, vol. 103, no. 5, pp. 1204–1208, 2006.

[104] M. Pozzo, C. Davies, D. Gubbins, and D. Alfè, "Transport properties for liquid silicon-oxygen-iron mixtures at Earth's core conditions," *Physical Review B - Condensed Matter and Materials Physics*, vol. 87, no. 1, p. 014110, 2013.

[105] H. M. Strong and R. E. Hanneman, "Crystallization of Diamond and Graphite," *Journal of Chemical Physics*, vol. 46, no. 9, pp. 3668–3676, 1967.

[106] A. Sorkin, J. Adler, and R. Kalish, "Nucleation of diamond from liquid carbon under extreme pressures : Atomistic simulation," *Physical Review B*, vol. 74, no. 6, p. 064115, 2006.

[107] W. H. Gust, "Phase transition and shock-compression parameters to 120 GPa for 3 types of graphite," *Physical Review B*, vol. 22, no. 10, pp. 4744–4756, 1980.

[108] C. J. Mundy, A. Curioni, N. Goldman, I. F. Kuo, E. J. Reed, L. E. Fried, and M. Ianuzzi, "Ultrafast transformation of graphite to diamond: An ab initio study of graphite under shock compression," *Journal of Chemical Physics*, vol. 128, no. 18, 2008.

[109] V. L. Deringer, D. M. Proserpio, G. Csányi, and C. J. Pickard, "Data-driven learning and prediction of inorganic crystal structures," *Faraday Discussions*, vol. 211, pp. 45–59, 2018.

[110] S. Plimpton, "Fast Parallel Algorithms for Short – Range Molecular Dynamics," *Journal of Computational Physics*, vol. 117, no. June 1994, pp. 1–19, 1995.

[111] E. Bitzek, P. Koskinen, F. Gähler, M. Moseler, and P. Gumbsch, "Structural relaxation made simple," *Physical Review Letters*, vol. 97, no. 17, p. 170201, 2006.

[112] C. J. Pickard, "Predicted Pressure-Induced s -Band Ferromagnetism in Alkali Metals," *Physical Review Letters*, vol. 107, no. 8, p. 087201, 2011.

[113] R. J. Needs and C. J. Pickard, "Perspective: Role of structure prediction in materials discovery and design," *APL Materials*, vol. 4, no. 5, 2016.

[114] Y. Kumeda and D. J. Wales, "Ab initio study of rearrangements between C60 fullerenes," *Chemical Physics Letters*, vol. 374, no. 1-2, pp. 125–131, 2003.

[115] D. J. Wales, "Global Optimization of Clusters, Crystals, and Biomolecules," *Science*, vol. 285, no. 5432, pp. 1368–1372, 1999.

[116] P. J. Harris and S. C. Tsang, "High-resolution electron microscopy studies of non- graphitizing carbons," *Philosophical Magazine A: Physics of Condensed Matter, Structure, Defects and Mechanical Properties*, vol. 76, no. 3, pp. 667–677, 1997.

[117] P. J. Harris, "New perspectives on the structure of graphitic carbons," *Critical Reviews in Solid State and Materials Sciences*, vol. 30, no. 4, pp. 235–253, 2005.

[118] P. J. F. Harris, "Structure of non-graphitising carbons," *International Materials Reviews*, vol. 42, no. 5, pp. 206–218, 2014.

[119] X. Dou, I. Hasa, D. Saurel, C. Vaalma, L. Wu, D. Buchholz, D. Bresser, S. Komaba, and S. Passerini, "Hard carbons for sodium-ion batteries: Structure, analysis, sustainability, and electrochemistry," *Materials Today*, vol. 23, no. March, pp. 87–104, 2019.